University of Alberta

Observation of Exclusive Charmonium Production and $\gamma\gamma \rightarrow \mu^+\mu^-$ in $p\bar{p}$ Collisions at $\sqrt{s}$ =1.96 TeV

by

Long Zhang

A thesis submitted to the Faculty of Graduate Studies and Research
in partial fulfillment of the requirements for the degree of

Master of Science

Department of Physics

Edmonton, Alberta
Fall 2008

Library and
Archives Canada

Published Heritage
Branch

395 Wellington Street
Ottawa ON K1A 0N4
Canada

Bibliothèque et
Archives Canada

Direction du
Patrimoine de l'édition

395, rue Wellington
Ottawa ON K1A 0N4
Canada

Your file Votre référence
ISBN: 978-0-494-47453-2
Our file Notre référence
ISBN: 978-0-494-47453-2

NOTICE:
The author has granted a non-exclusive license allowing Library and Archives Canada to reproduce, publish, archive, preserve, conserve, communicate to the public by telecommunication or on the Internet, loan, distribute and sell theses worldwide, for commercial or non-commercial purposes, in microform, paper, electronic and/or any other formats.

The author retains copyright ownership and moral rights in this thesis. Neither the thesis nor substantial extracts from it may be printed or otherwise reproduced without the author's permission.

AVIS:
L'auteur a accordé une licence non exclusive permettant à la Bibliothèque et Archives Canada de reproduire, publier, archiver, sauvegarder, conserver, transmettre au public par télécommunication ou par l'Internet, prêter, distribuer et vendre des thèses partout dans le monde, à des fins commerciales ou autres, sur support microforme, papier, électronique et/ou autres formats.

L'auteur conserve la propriété du droit d'auteur et des droits moraux qui protège cette thèse. Ni la thèse ni des extraits substantiels de celle-ci ne doivent être imprimés ou autrement reproduits sans son autorisation.

In compliance with the Canadian Privacy Act some supporting forms may have been removed from this thesis.

While these forms may be included in the document page count, their removal does not represent any loss of content from the thesis.

Conformément à la loi canadienne sur la protection de la vie privée, quelques formulaires secondaires ont été enlevés de cette thèse.

Bien que ces formulaires aient inclus dans la pagination, il n'y aura aucun contenu manquant.

Canada

Abstract

We observed exclusive $\mu^+\mu^-$ production, with $3 < M(\mu^+\mu^-) < 4$ GeV/c^2 in proton-antiproton collisions at $\sqrt{s} = 1.96$ TeV, using 1.48 fb^{-1} of integrated luminosity taken by the Run II Collider Detector at Fermilab. The event signature requires two oppositely charged muons, each with transverse momentum $P_T > 1.4$ GeV/c and pseudorapidity $|\eta| < 0.6$, with no other particles detected in the event. The events are collected by a muon-plus-track trigger during CDF Run II period 1 to 11 (run number 190697 – 237795). The J/ψ and the ψ' meson productions are prominent, on a small continuum consistent with the QED two-photon process $\gamma\gamma \rightarrow \mu^+\mu^-$. The exclusive vector meson production channel $\gamma\mathbb{P} \rightarrow J/\psi$ or $\psi' \rightarrow \mu^+\mu^-$ is observed here for the first time in hadron-hadron collisions. We discuss the background from exclusive $\mathbb{P}\mathbb{P} \rightarrow \chi_c \rightarrow J/\psi + \gamma$ production where the low energy photon is undetected. The measured cross section for the exclusive QED continuum process $\gamma\gamma \rightarrow \mu^+\mu^-$ is 2.6 ± 0.5 pb, consistent with theoretical prediction. The exclusive photoproduction cross-sections determined for the processes $\gamma\mathbb{P} \rightarrow J/\psi \rightarrow \mu^+\mu^-$ and $\gamma\mathbb{P} \rightarrow \psi' \rightarrow \mu^+\mu^-$ are 531.2 ± 48.9 pb and 106.8 ± 41.1 pb, respectively.

Acknowledgment

First, thank Professor James Pinfold, Dr. Mike Albrow and Andrew Hamilton for helping me to get into the analysis at the very beginning, and encouraging me all the way. Especially, this analysis benefits a lot from the exclusivity cuts that Andrew Hamilton pioneered in his exclusive electron pair analysis.

The MiniPlug Calorimeter and BSC counters provided by the Rockefeller group are essential to this analysis. Koji Terashi, when he was in CDF Rockefeller group, helped me work through the standalone detector simulation on LPAIR and STARLIGHT Monte Carlo events, and helped me clear many concepts related to the exclusive efficiency of this analysis. His help is a unique resource, without which I cannot finish the analysis.

I truly appreciate the contribution from Vyacheslav Krutelyov of the B physics group, who has performed the measurement of very low P_T (down to 1.4 GeV/c) CMU Level 1 muon trigger efficiency, uniquely for this analysis.

I would like to thank Professor Joakim Nystrand for providing the STARLIGHT Monte Carlo event samples, and for calculating the theoretical cross sections used in this analysis. I would like also thank the Durham theory group (Khoze and Stirling) for the CHIC Monte Carlo program and many consultations on theoretical aspects.

Finally I thank the hard work of the QCD group conveners and the analysis reviewers for carefully examining this analysis.

Table of Contents

1. Introduction

This thesis presents the observation of exclusive muon pair events collected by a CDF muon plus track trigger during Tevatron Run II period 1 to 11 (run 190697 – 237795). Each event has the final state of a muon pair and nothing else observable in CDF detector. The results of exclusive muon pair events come from a continuum contribution of two-photon exchange process ($\gamma\gamma \rightarrow \mu^{+}\mu^{-}$) and the photoproduction of J/Ψ and $\Psi^{'}$ then decaying into muon pairs ($\gamma\mathbb{P} \rightarrow J/\Psi$ or $\Psi^{'} \rightarrow \mu^{+}\mu^{-}$). The cross sections of these processes are measured and compared with theoretical predictions.

The first part of the thesis is a brief description of the Standard Model of particle physics as well as some topics beyond the Standard Model. The emphasis is on the mechanism of exclusive interactions. The second part is devoted to description of the accelerator and detector, with more details of the various issues of muon detection. The third part of the thesis includes the analysis procedures and measured results, with comparisons to the Monte Carlo predictions.

2. Theoretical Models

2.1 Standard Model of Elementary Particles

The Standard Model of elementary particles [1] is the theoretical base of current experimental particle physics. It describes 3 (electromagnetic force, weak force, strong force) of the 4 known fundamental forces. It comes in the mathematical form of relativistic quantum field theory, which is consistent with the principles of both quantum mechanics and special relativity. It actually contains two major quantum field theories - electroweak theory [2] and quantum chromodynamics [3], and presents them via the gauge group of $SU(3)_{C}\times SU(2)_{W}\times U(1)_{Y}$. To date most experimental tests agreed with Standard Model predictions. In this section, the Standard Model is briefly described, in order to understand the mechanisms of the exclusive interactions discussed later in this thesis.

2.1.1 Standard Model

The Standard Model (SM) of elementary particles describes the fundamental particles that constitute the visible matter in the universe and describes the interactions between the fundamental particles. According to SM the fundamental particles are divided into fermions (spin 1/2), gauge bosons (spin 1) and a Higgs boson (spin 0). Fermions are also called "matter particles" since they are the particles from which matter is composed. Twelve different fermions are known to exist, six of them are quarks (up, down, charm, strange, top, bottom), the other six are leptons (electron, muon, tau) and their corresponding neutrinos. There are also 12 anti-particles, one for each of the 12 fermions. Bosons, on the other hand, are often called "force mediation particles". The Standard Model explains interactions between matter particles as a result of gauge boson exchange, when a boson is exchanged between two fermions, it's equivalent to a force between the fermions. There are 6 kinds of boson in the SM: $W^{\pm}, Z, \gamma$, g and Higgs boson, where γ is the photon, g represents 8 types of gluons, $W^{\pm}$ and Z bosons have no other names and they are just called as their names appear. The SM divides elementary particles into three generations. Between different generations, particles differ only by their mass, all interactions and flavor quantum numbers are identical. Each generation consists of two leptons (one with electric charge -1, electron-like; and one neutral, neutrino-like.) and two quarks (one with charge $-1/3$, down-type; and one with charge +2/3, up-type). Each member of a higher generation has greater mass than the corresponding particle of the previous generation. For example: the electron of the 1st generation has a mass of 0.511 MeV/c^2, the muon of the 2nd generation has a mass of 106 MeV/c^2, and the tau of 3rd generation has a mass of 1777 MeV/c^2. All ordinary atoms (electrons, protons, neutrons) in the world are made of the 1st generation particles. The 2nd and 3rd generations of charged particles do not exist in normal matter and are only seen in extremely high-energy conditions. The picture on next page shows the particle table of Standard Model.

The SM classifies the fermions and gauge bosons according to interaction types. The electromagnetic (EM) interaction is the force between charged fermions, the force mediation particle is the γ (photon), which is massless. EM interactions of charged particles are described by the theory of quantum electrodynamics (QED) [4]. Because of its precise predictions of quantities like the magnetic moment of electron and Lamb shift of the hydrogen atom, QED has been proved to be an extremely successful theory.

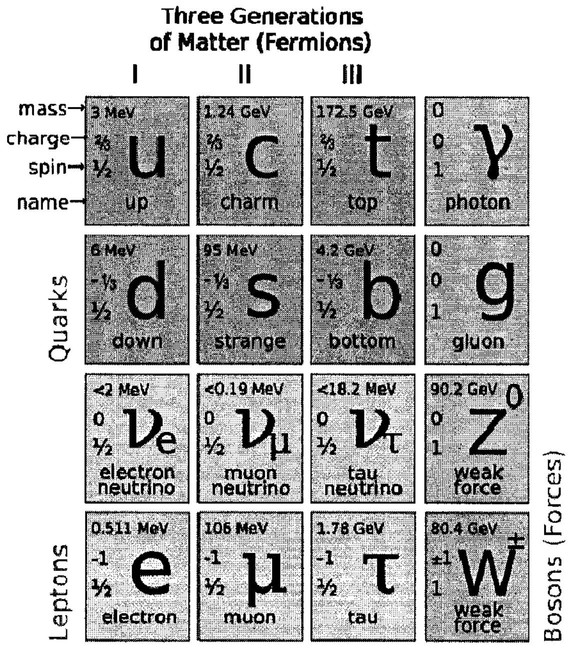

Particle table of Standard Model (Higgs boson is not in the table)

The weak interaction is the one that involves all left-hand leptons and quarks. The force mediation particles are $W^{\pm}$ and Z bosons. An electron (or muon or tau) can emit or absorb a W boson and convert to its corresponding neutrino. Similarly a down-quark can emit or absorb a W boson and convert to an up-quark. Because those two kinds of interaction are mediated by the charged $W^{\pm}$ boson, they are called charged current interactions. There is also the neutral current interaction which refers to either a lepton or a quark emits or absorbs a neutral Z boson. The weak interaction is the only one which affects neutrinos, and it violates parity symmetry because it only acts on left-handed particles and right-handed anti-particles. Because the $W^{\pm}$ carry electric charge of ± 1, they take part in the electromagnetic interactions. The $W^{\pm}$, Z bosons and the photon are grouped together and described by the Electroweak theory.

The strong force is experienced between quarks, anti-quarks and gluons, and is mediated by eight gluons. The gluons and strong force are described by the theory of quantum chromodynamics (QCD). Gluons are massless and carry color charges. The gluon is its own anti-particle. Quarks also carry color charge. The confinement behavior of strong force results in the quarks being bound together, forming color-neutral composite particles, called hadrons. The hadrons comprised of quark-antiquark pair states are called mesons, and those hadrons corresponding to three-quark states are called baryons. The hadrons with $b\bar{b}$ and $c\bar{c}$ constituent quarks are referred to as heavy flavor hadrons: b-hadrons and charm hadrons, respectively.

Mathematically, quantum field theory is the framework of SM. The SM contains two major field theories — quantum chromodynamics and quantum electroweak theory, which are related to gauge fields of $SU(3)_C$ and $SU(2)_W \times SU(1)_Y$ groups for strong and electroweak interactions, respectively. The gauge fields correspond to the particles mediating the corresponding interactions, and define the vector field content of SM: gluons for $SU(3)_C$; $W^{\pm}, Z, \text{and}\, \gamma$ for $SU(2)_W \times SU(1)_Y$. The Higgs field is the only scalar field in the model. Initially, all the particles in the model are massless, and masses are generated as a result of interaction with a scalar (Higgs) field via a spontaneous electroweak symmetry breaking (EWSB) mechanism. This mechanism also defines the electromagnetic (massless photon field γ or A_μ) and the weak (massive charged fields $W^{\pm}$ and a neutral field Z) components of the original unbroken $SU(2)_W \times SU(1)_Y$ electroweak symmetry.

2.1.2 Beyond the Standard Model

To date most confirmed results in the field of particle physics are consistent with the Standard Model. Despite the success of the Standard Model, there are some problems that SM does not give answers. Such problems include: no explanation of the gravitational force; no explanation of the generational structure of SM; no explanation for charge conservation; neutrino oscillations (direct evidence for non-zero neutrino mass); no explanation of the dark matter in the universe and there are 21 free parameters of the SM. All those unsolved problems make SM an incomplete model.

Neutrino oscillation [5], i.e. the observation of neutrino flavor change with distance/time, unequivocally suggests that neutrinos have mass. The dark matter problem is related to the cosmological observation which shows that of all the matter in the universe only a fraction consists of the particles included in the Standard Model. There is a substantial need to extend the Standard Model. The models extending the SM are driven by a number of theoretical concepts not included in the SM, as well as by a desire to explain the experimental observations mentioned above. The most discussed concepts outside the Standard Model include: super symmetry, grand unification, Yukawa or gauge hierarchy problem, string theory, and more [6].

Supersymmetry (SUSY) [7] is the symmetry between bosons and fermions. A supersymmetric theory has the same number of bosonic and fermionic degrees of freedom, and each particle has a corresponding superpartner. Mathematically supersymmetry arises from the requirement that the theory should be invariant under the transformations that convert bosons to fermions, and vice versa. These are global, not local, transformations of the fields, and can be considered as an extension to the Poincare group transformations.The names of the superpartners to fermions have a prefix “s”, for example squarks, and the names of the superpartners to bosons have a suffix “ino” for example gluino. SUSY is theoretically attractive because it provides a natural solution to the gauge hierarchy problem. The gauge hierarchy problem is usually connected to the Higgs field in the SM in application to the higher energy scales. The Higgs mass gains a correction proportional to the mass-squared of the fields that the Higgs interacts with.

Grand unified theory (GUT) [8][9] attempts to unify the electroweak and strong interactions. It describes the SM gauge group by a single simple gauge group in which all the particles can be combined in a single representation (one for matter and one for the gauge fields). This group symmetry is then considered to be broken below some energy scale (the GUT scale) which gives rise to the $SU(3)_C \times SU(2)_W \times U(1)_Y$. This is mostly inspired by the fact that the three running coupling constants of the SM do seem to converge to roughly the same value at the scale of around 10^{16} GeV. The common consequences of the GUTs are lepton and baryon number violation and the possibility of proton decay as a result.

The string theories [10], which generally require supersymmetry, describe particles as extended objects, one-dimensional strings. The consistent string theories that include both bosons and fermions are supersymmetric. They are formulated in a higher dimensional space time: the most theoretically attractive M theory is defined in 11 dimensions. M theory (or superstring theory) are candidates for a Theory of Everything (ToE) that includes gravity, electroweak, and strong forces in terms of quantized gauge fields.

2.2 Exclusive Interactions

In particle collisions, the term "exclusive interaction" refers to those hadron-hadron interactions in which the hadrons do not dissociate, and escape the interaction intact. At CDF the hadrons of interest are protons and antiprotons. In general, exclusive interactions can be represented as: $p + \bar{p} \rightarrow p + X + \bar{p}$, where X is the central system produced in the interaction. The central system of the interactions observed in this thesis is just a pair of muons: $\mu^+\mu^-$. In the particle detectors exclusive interactions are often observed as events with rapidity gaps (rapidity regions where no particle is observed).

In elastic single diffractive scattering, the scattered proton causes an energy-momentum exchange, but not of quantum numbers. In Regge phenomenology theory [11] such processes are described by exchange of a "pomeron" ($\mathbb{P}$), named after Russian theoretician Isaak Yakovlevich Pomeranchuk (1913-1966). In QCD theory the pomeron is color-singlet with vacuum quantum numbers, it is generally defined as a hadron-like object with gluon content. The concept of pomeron comes into 2 of the 3 kinds of exclusive interactions involved in this thesis. The 3 kinds of exclusive interactions involved in this thesis are mediated by: the exchange of two photons, or photon-pomeron fusion, or the exchange of two pomerons.

The study of the reaction $p + \bar{p} \rightarrow p + \mu^+\mu^- + \bar{p}$ at CDF is in progress. At low mass the exclusive $\mu^+\mu^-$ final state can be produced in three ways as mentioned above, via the decay of the J/ψ or ψ' resonance and from continuum QED (two photon) interactions. The cross-section for the latter is theoretically very well known and provides a test of our exclusivity criteria. Exclusive vector mesons V can be produced by photon-pomeron ($\gamma\mathbb{P}$) fusion (photoproduction). This process has been measured at HERA in ep-collisions but not, up to now, in hadron-hadron collisions. In principle, such final states can also be produced by odderon-pomeron fusion, where the odderon is a CP-odd partner to the pomeron ($\mathbb{P}$). However, as yet, there is no firm evidence for the existence of the odderon. The main background to exclusive J/ψ production is exclusive χ_c production by double pomeron exchange, followed by $\chi_c^0 \rightarrow J/\psi(\rightarrow \mu^+\mu^-) + \gamma$ where the photon, with maximum energy ~500 MeV, is undetected. We are also studying the higher mass exclusive process, $p + \bar{p} \rightarrow p + (\Upsilon \rightarrow \mu^+\mu^-) + \bar{p}$. An important physics interest here is that photoproduction measures V-p elastic scattering where V is a vector meson with the constituent quarks heavy enough for perturbative QCD to be relevant. Another issue is the search for evidence of odderon exchange. Also, at the LHC exclusive $\mu^+\mu^-$ from the J/ψ, ψ' and Υ provides a powerful tool for calibrating planned forward proton spectrometers. In addition, exclusive continuum muon pair production provides a physics process with a relatively well known cross-section for luminosity determination.

The Feynman diagrams for the three main types of exclusive process studied at CDF are shown in Figure 1. Additional processes would involve the odderon, for example pomeron odderon fusion. In principle, this process would also contribute to J/ψ and ψ' exclusive production observed at the Tevatron at some level.

Central exclusive production at the Large Hadron Collider (LHC), where central masses up to several hundred GeV are attainable, opens up new central exclusive channels, X = H, W^+W^-, ZZ etc., where H is a Higgs boson. The deployment of forward proton detectors at 200 m and 420 m from the interaction point of ATLAS and CMS, in order to exploit this and other forward physics scenarios, is currently under consideration.

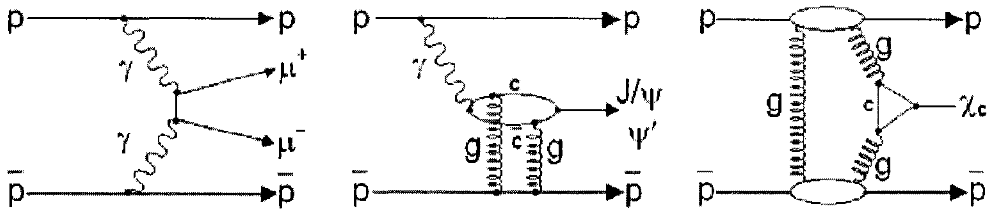

Figure 1: The Feyman diagrams for the three main types of exclusive process relevant to this thesis: two photon interactions (left) that contribute to the $\mu^+\mu^-$ continuum; photon-pomeron fusion or photoproduction (middle) that produce the vector meson $\mu^+\mu^-$s; and, double pomeron exchange (right) that gives rise to the χ_c background.

2.2.1 QED mediated two-photon exchange

QED mediated exclusive interactions are also called "two-photon processes". Exclusive electron pair production has been observed at CDF [12], and the measured cross section agreed with theoretical prediction. Measuring the cross section of QED mediated exclusive muon pair production is one of the main results reported in this thesis.

2.2.2 QCD mediated Charmonium production

Charmonium is defined as the bound state of $c\bar{c}$, i.e. a charm-quark and an anti-charm-quark. The 2 kinds of exclusive interactions involving pomerons discussed in this thesis are both coming from the decay of charmonium states, more specifically the J/Ψ and Ψ' meson states. It is necessary to describe the mechanism of charmonium production and it's energy levels in order to understand the 2 processes better.

Generally “quarkonium” means a flavorless meson whose constituents are a quark and its own anti-quark. Naively there should be six kinds of quarkonium states as there are six kinds of quarks. It has been observed in experiments the mixtures of the light quark quarkonium states, where light quark refers to up, down and strange quarks. Because of the very high mass of the top quark, a well-defined toponium state has not been observed in experiments. The top quarks decays via electroweak interaction before a $t\bar{t}$ bound state can form. Thus, usually, quarkonium refers only to ***charmonium*** ($c\bar{c}$ bound state) and ***bottomonium*** ($b\bar{b}$ bound state). In high energy $p\bar{p}$ collisions the Ψ mesons (Ψ represents a set of mesons: J/Ψ, Ψ', Ψ'', etc) are charmonium states, and $\Upsilon(1s)$, $\Upsilon(2s)$ and $\Upsilon(3s)$ are bottomonium states.

When the $b\bar{b}$ pair bound state is produced, after fragmentation it may form a B hadron, and the hadron may decay to J/Ψ or χ_c meson plus *anything*, this process is referred as B production which is not the focus of this thesis.

When the $c\bar{c}$ pair bound state is produced in $p\bar{p}$ hard scattering, it could: (1) directly produce a Ψ meson which could be J/Ψ or Ψ' or Ψ''; (2) directly produce a χ_c meson, and the χ_c meson will electromagnetically decay to J/Ψ meson plus a photon, this process only contributes to the J/Ψ meson production, not Ψ' or Ψ''. The charmonium production is sometimes called *prompt* if the point at which the $c\bar{c}$ state is produced cannot be resolved from the interaction point of the proton beams. In this thesis, the cross sections of direct J/Ψ and Ψ' production are measured. The direct χ_c production appears as a significant background process for the direct exclusive J/Ψ production, this is because the photon from χ_c decay is soft, with maximum energy of ~500 MeV, which is often experimentally difficult to distinguish from noise at CDF.

The charmonium system (actually all quarkonium states) is similar to that of the positronium system (a system consisting of e^+ and e^-, the orbit and energy levels of e^+ and e^- are similar to those of the hydrogen atom). Positronium is bound together by exchanging soft photons, and the charmonium is bound together by exchanging soft gluons. The quantum numbers used to describe positronium includes the angular momentum quantum number (from rotational invariance of the potential) and the radial quantum number, and quark-quark potential has similar properties so similar quantum numbers exists for the charmonium. Figure 2 shows the energy levels of the charmonium states. The charmonium state can decay "electromagnetically", where either the $c\bar{c}$ pair annihilates into virtual photon or emits a real photon. These decays form a large fraction of the decays of charmonium states.

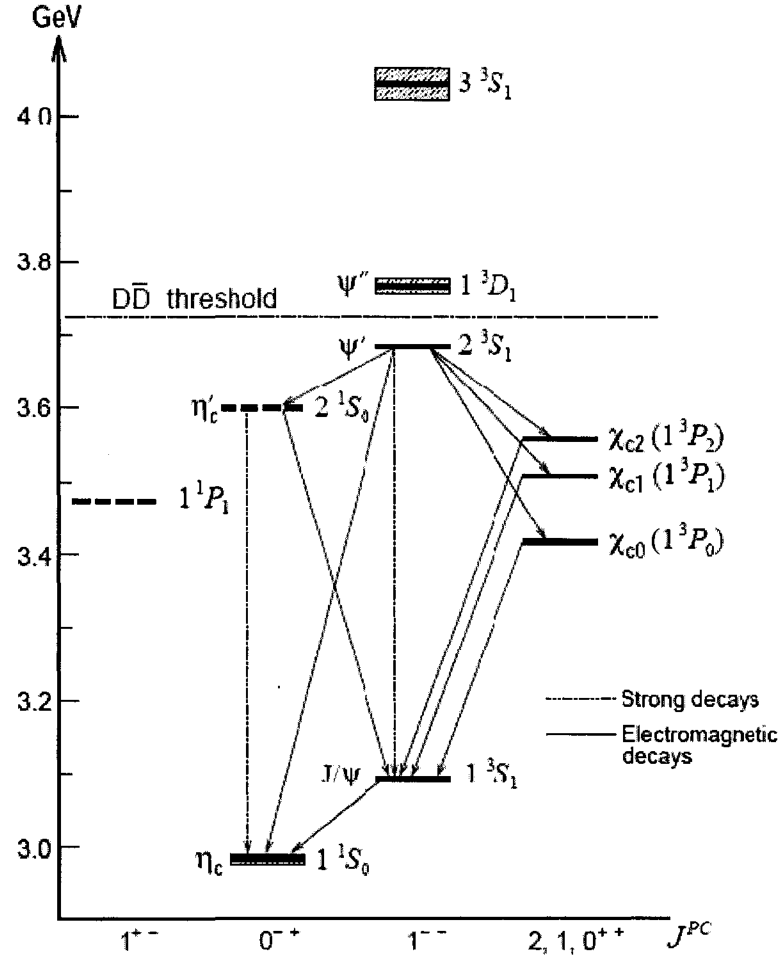

Figure 2. Energy levels of the charmonium states. [13]

The lowest energy level of charmonium is the η_c, in which the $c\bar{c}$ pair is in an S wave state, with quark spins anti-parallel. The 2nd lowest state is the J/Ψ (or $\Psi(1S)$), in which the $c\bar{c}$ pair is in an S wave state, with quark spins parallel. The next excited S wave state is the Ψ' (or $\Psi(2S)$), and the highest energy state, the Ψ''. The P wave states with parallel spins are denoted as χ_{cJ}, where J = 0, 1, 2 is the total angular momentum, and χ_c is actually a generic notation for any χ_{cJ}. A χ_c state could electromagnetically decay to lower J/Ψ state with emitting a photon, thus contributes to prompt J/Ψ production. Other excited states, such as the P wave spin singlet and D wave states, are expected not to give significant contribution to the production of Ψ mesons.

In summary, there are three exclusive processes discussed in this thesis, they are:

1. QED mediated exclusive two-photon exchange process: $\gamma\gamma \to \mu^+\mu^-$. The cross section measurement of this process is reported in this thesis.
2. Prompt J/Ψ and Ψ' meson production from the charmonium states, where the J/Ψ and Ψ' decay to $\mu^+\mu^-$. The measurement of the cross sections of these two processes is reported in this thesis.
3. Prompt χ_c meson production from the charmonium states, where the χ_c subsequently decays to a J/Ψ plus a photon, and the J/Ψ further decays to $\mu^+\mu^-$.

The final state of (1) and (2) is experimentally the same: $p + \bar{p} \to p + \mu^+\mu^- + \bar{p}$. These are very clean signal events with only two muons in the final state, and the beam protons do not break up. However the final state of (3) contains an additional low energy photon, which is difficult to distinguish from background noises. Thus this process serves as an important background to (2). Estimating the χ_c background is a challenging aspect of this analysis.

2.3 Monte Carlo Event Generators

The STARLIGHT Monte Carlo [14] is used to model both $\gamma\gamma \rightarrow \mu^+\mu^-$ (QED) and the exclusive photoproduction of the J/Ψ and Ψ' vector mesons. It uses a phenomenological model based on input photon-nucleon data: parametrized from results at HERA and fixed target experiments. A Weizsacker-Williams photon spectrum is used in the QED calculation of the two-photon processes. The LPAIR Monte Carlo program [15] is also used to model $\gamma\gamma \rightarrow \mu^+\mu^-$ production and agrees well with STARLIGHT. LPAIR is a matrix element simulation of two photon production of fermion pairs with incoming beams of electrons, positrons, protons, and antiprotons. The code presents a numerically stable program for all collision energies through a reformulation of the basic phase space integrals. The CHIC Monte Carlo [16] program is used to simulate χ_c production and the χ_c decay to J/Ψ plus a photon, where the J/Ψ further decays to $\mu^+\mu^-$. Essentially, this Monte Carlo program parameterizes the cross sections calculated in the Khoze et al. 2004 paper [17]. The non-perturbative pomeron parameters are also taken from Reference [17].

Three categories of two photon collisions from the incoming proton anti-proton beams of the Tevatron can be simulated with LPAIR. The elastic-elastic exclusive process is the generator configuration used to simulate the expected signal for this analysis. The elastic-inelastic and inelastic-inelastic configurations are used to estimate the background from proton dissociation (due to $\gamma\gamma$ collisions, but not exclusive because of additional produced (forward) particles).

Finally, the simulation of the effects of the measurement in the CDF detector, on the Monte Carlo generated particles, is provided by CDF detector simulation [18] [19], CDFSim, a GEANT [20] based program.

3. Experimental Apparatus

The data for this analysis is taken from the Collider Detector at Fermilab (CDF) experiment located at the Fermi National Accelerator Laboratory (Fermilab), Batavia, Illinois, USA. In the following sections, I outline the Fermilab accelerator complex and the CDF II detector with its components.

3.1 The Accelerator – Tevatron Run II

Fermilab is the home of Tevatron, which is currently (before LHC operates) the world's highest energy collider. The Tevatron, with a circumference of about 6 km, was the world's first superconducting synchrotron, beginning operation in 1983. Two collision points on Tevatron host two $p\bar{p}$ colliding beam experiments: D0 and CDF. Both experiments took data during the 1980's and 1990's. Starting in 1996, both the accelerator and the experiments underwent significant upgrades. Data taking began again in 2001 with the upgraded accelerator and experiments.

The center-of-mass energy of the Tevatron proton and antiproton collisions is 1.96 TeV. The acceleration of proton and antiproton beams to 0.98 TeV is done in many stages in the accelerator. The rest of this section describes in detail the stages of the accelerator chain, which is illustrated in Figure 3. The other important parameter of colliders, the measure of the potential number of interactions for the colliding beams ("luminosity"), will be defined at the end of this section. Most of information provided in this section can be found in Run II Handbook [21].

Proton Source:

The starting point of the acceleration is the Cockcroft-Walton accelerator which is a source of 750 KeV negative hydrogen ions (H^-). The H^- ions enter a 150m long Linear Accelerator (Linac). The Linac uses a radio-frequency field, running at about 800 MHz, to further accelerate the H^- ions to an energy of 400 MeV. Upon leaving the

Linac, the H$^-$ ions enter into the Booster, the first synchrotron of the accelerator chain at Fermilab. During this process, the ions are passed through a carbon foil and the electrons are stripped, leaving the bare protons to be accelerated to 8 GeV in the 75m radius Booster. Protons emerge from the Booster in 84 bunches (1 bunch = 1 RF "bucket") spaced by about 19 ns. The aim of the Booster for Run II is to achieve a total intensity of 6x10^{10} protons per bunch, which is 20% improvement over Run I B (see section 3.2 for detailed periods of Run I B and Run II).

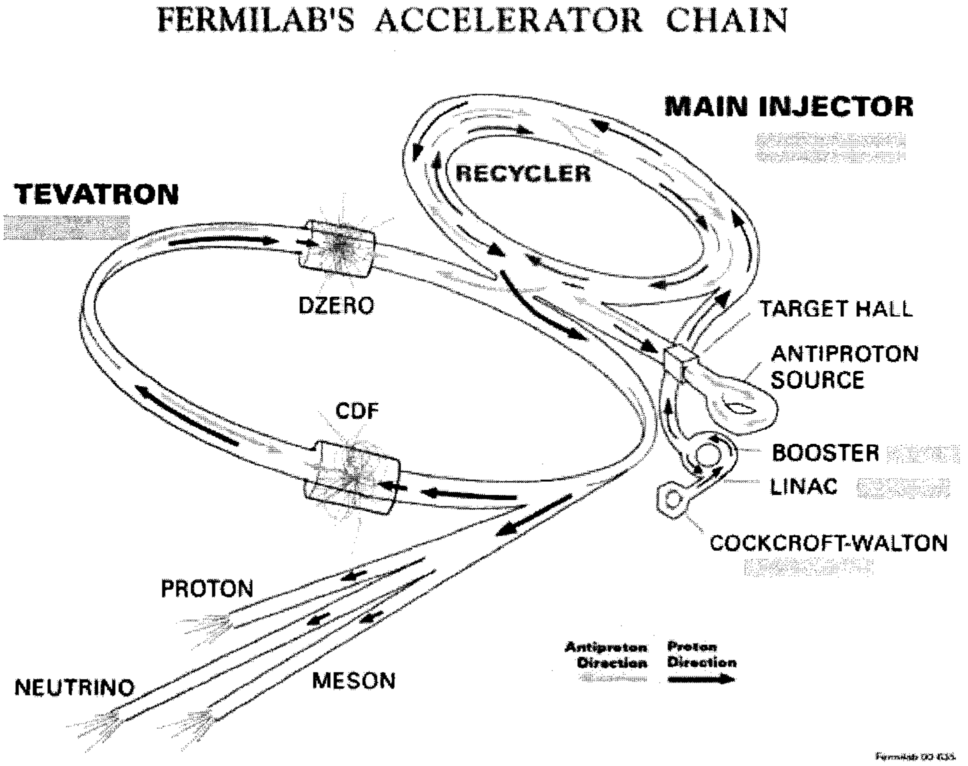

Figure3. The Tevatron Accelerator Chain

Main Injector:

The Tevatron's Main Ring, was incapable of meeting the luminosity requirements for Run II. The Main Injector, a synchrotron of about 3 km in circumference, was designed and built to overcome the limitation of the Main Ring and became operational in 1998. The Main Injector accelerates both protons and antiprotons from 8 GeV to 150 GeV (the "shot set-up" procedure).

Both beams are divided into bunches, which are finally injected into the Tevatron (36 bunches per beam in total), where they will be further accelerated to their final energy of 980 GeV.

Antiproton Production:

One major advantage of $p\bar{p}$ collider is that beams can circulate in opposite directions sharing the same magnet and vacuum system. One major challenge of using $\bar{p}$ beams is the difficulty of producing suitablly intense $\bar{p}$ beams. At Fermilab, the antiprotons are produced using the Main Injector protons. A proton pulse of 120 GeV is incident onto a nickel target to produce antiprotons. The produced antiprotons are collected and focused by a "lithium lens" and separated from the other by-products of the interactor, using a bending magnet. The system has a wide acceptance around $\bar{p}$ energy of 8 GeV. Exiting the collection lens, the antiprotons are bunched (preserving the bunch structure of the initial protons). However, they have a large spread of momentum in longitudinal and transverse directions. Before bringing them up to 150 GeV to prepare for proton collisions, they go through the process of stochastic cooling (Simone van der Meer was awarded the Nobel prize for invention of stochastic cooling in 1984). This task is performed in two steps: the $\bar{p}$ beam is transformed into a continuous beam and cooled both transversely and longitudinally in the Debuncher ring, and the antiprotons are further cooled and "stacked" in the Accumulator. The stacking of anti-protons takes between half or a full day depending on the desired beam intensity. At this point, the antiprotons are still 8 GeV, but with a momentum spread smaller than 1% and are rebunched. When a sufficient number of antiprotons is available, they are sent either to the Main Injector for further acceleration to 150 GeV or to the Recycler, which is described below. The improvements to the Debuncher and Accumulator stochastic cooling systems and the increase in the number of protons per pulse from the Main Injector along with a faster repetition rate are designed to increase the stacking rate by at least a factor of four in Run II as compared to that of Run I.

Recycler:

The Recycler Ring is installed in the Main Injector enclosure as a storage ring for antiprotons. It is used as a post-Accumulator ring. Its main purpose is to recycle the antiprotons which are not used at the end of the Tevatron stores (about 75% of the original injection quantity). At the end of a store, the antiprotons, instead of being dumped as in Run I, will be decelerated, re-cooled, stored and will be sent back to the Main Injector to be used again in the next store. This recycling procedure essentially provides a factor of two in luminosity attainable by the accelerator.

Tevatron:

The final stage for the acceleration for the $p\bar{p}$ beams is the 6 km long Tevatron ring. The 36 proton and antiproton bunches are received from the Main Injector at 150 GeV. The general steps of a "shot setup" (the procedure of increasing beam energy from 150 GeV to 980 GeV and getting ready for collisions at CDF and D0) can be outlined in the following steps.

- Beam Injection: The protons are sent into the F section of the Tevatron in 36 coalesced bunches. At this time, the Tevatron magnets are already set to circulate 150 GeV energy beams in anticipation of the injection. The antiprotons are loaded after all the protons are injected. Before antiproton injection, a set of electrostatic separators are used to create a pair of non-intersecting closed helical orbits with the protons circulating on one strand of the helix and antiprotons on the other. This provides transverse separation of the proton and antiproton bunches as they pass each other and reduces the beam-beam tune shift from head-on collisions. The tune shifts arise from beam-beam interactions due to the protons' electromagnetic field affecting antiprotons traveling in opposite directions.
- Acceleration: Both protons and antiprotons circulate in three trains of 12 bunches with bunches in each group spaced 396 ns and the three trains are separated by about 2.6 μs ("abort gaps"), as shown schematically in

Figure.4. The beams are accelerated up to 980 GeV each.

- Low Beta Squeeze: After the beams are accelerated to 980 GeV, the beta in the CDF and D0 interaction regions is reduced from about 2 m to 30 cm. The transverse size is reduced from about 1 mm to about 25 μm. The change in the Tevatron lattice is obtained by ramping up the currents in the low-beta quadrupole magnets at two sides of the detectors in the collision hall.

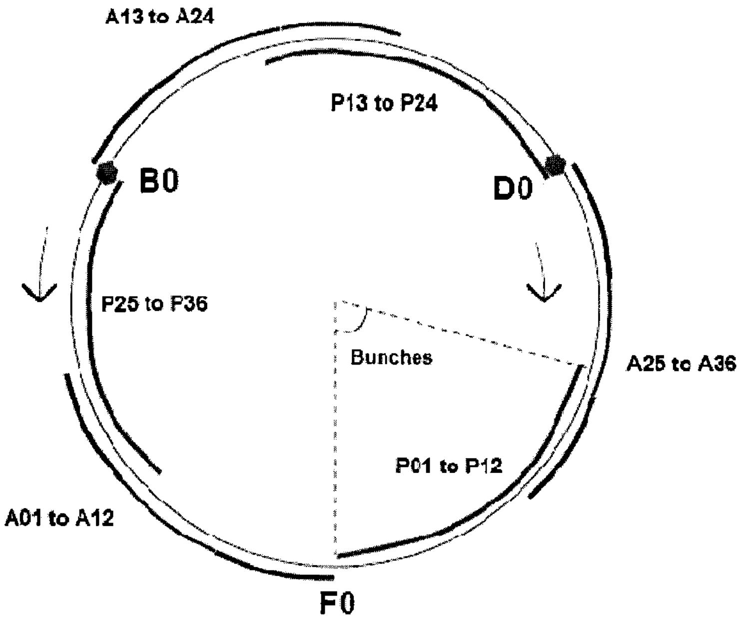

Figure 4. Three "trains" of proton and three "trains" of antiproton, each train is divided into 12 bunches.

- Beam Halo Scraping: The Tevatron beams begin to produce luminosity when the beams have been brought into collisions. At this stage, the proton and antiproton beam halo are scraped to reduce backgrounds in the detectors. This operation is usually done automatically using the scraping collimators around the ring.

Once the beams are ready for data taking, CDF and D0 detectors initialize their luminosity counters and turn on their detectors for taking data during the Tevatron store until the store is dumped or aborted. By the middle of 2008, the instantaneous luminosity at the beginning of a store was routinely pushed to about 300 ×

$10^{30}cm^{-2}sec^{-1}$. Figure 5 [22] shows the total integrated luminosity achieved by store numbers (left) and by date (right).

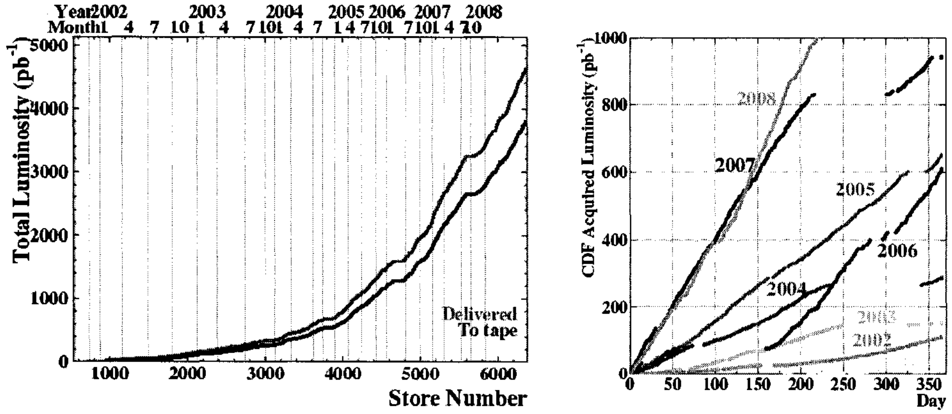

Figure 5. Total integrated luminosity achieved

by store numbers (left) and by date (right)

3.2 The CDF detector

The Collider Detector at Fermilab (CDF) is a cylindrical-shaped, general-purpose apparatus located at the B0 interaction region of the Tevatron and is designed to study particles coming from the pp̄ collisions. The CDF experiment went through a series of data taking periods starting from the date the first collisions were produced and detected in October, 1985. The history of CDF data taking is summarized in Table 1. The CDF and D0 experiments provided, in 1995, the first evidence for the existence of the top quark using Run I data [23]. The upgrade preparations for CDF Run II started in 1996. An isometric view of the CDF II detector can be seen in Figure 6.

CDF uses a cylindrical system of coordinates as is shown in Figure 7. The origin of the coordinate system is the interaction point. The +z axis points along the proton beam direction and the +y axis points upward (perpendicular to the Tevatron ring). Thus, according to the right-hand rule, the +x axis points radially outward from the Tevatron ring center. From the proton's point of view coming into the CDF detector (going eastward), the +x-axis would be the 9 o'clock with azimuthal angle, ϕ, increasing in the clockwise direction. The polar angle, θ, is measured from the +z direction. However in experimental particle physics people use another quantity, call pseudo-rapidity, instead of polar angle θ. Pseudo-rapidity is defined as: $\eta = -\ln(\tan\frac{\theta}{2})$. It is a good approximation of the true rapidity, which is defined as: $y = \frac{1}{2}\ln(\frac{E+p_z}{E-p_z})$

Run	Period	Integrated Luminosity (pb^{-1})
	1987	0.025
Run 0	1988 – 1989	4.5
Run I A	1992 – 1993	~19
Run I B	1994 – 1996	~90
Run II A	2001 – 2003	~200
Run II B	2003 – now	

Table 1. CDF detector Run I and Run II periods

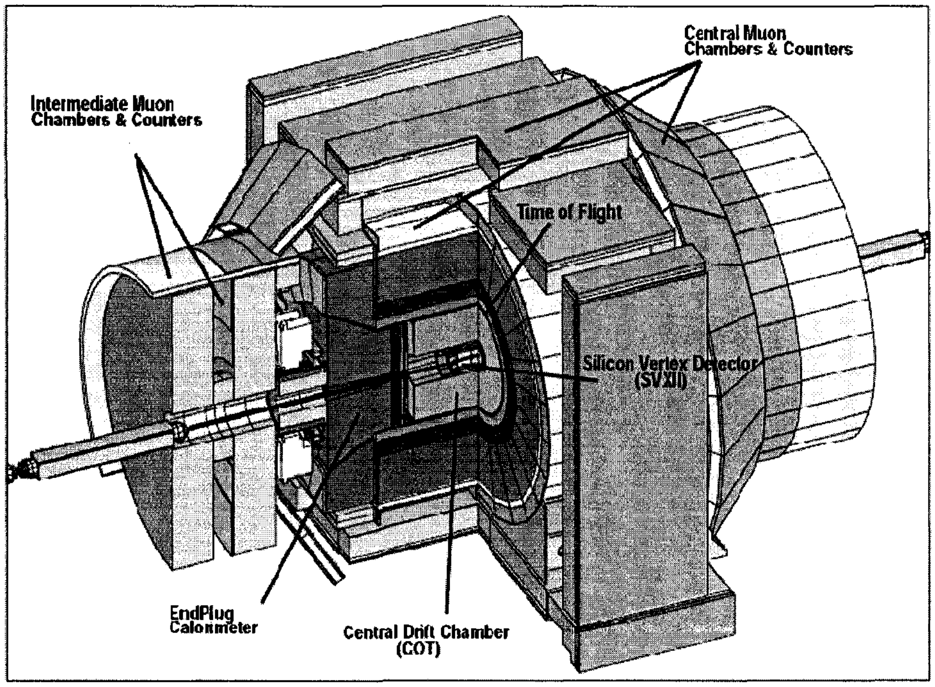

Figure 6. Isometric view of the CDF II detector

The following subsections outline the detector parts starting from the innermost regions and progressing radially outward.

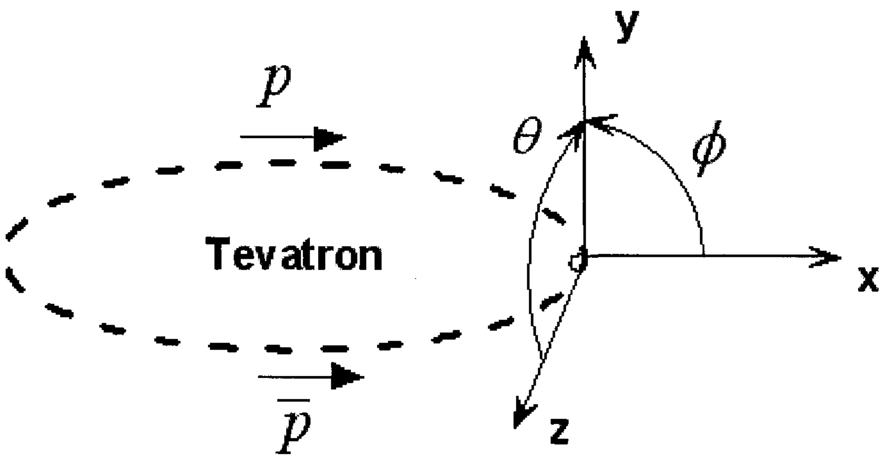

Figure 7. CDF coordinate system

3.2.1 Tracking Systems

The CDF detector has a powerful magnetic spectrometer consisting of several detector systems. The inner core is a set of silicon strip detectors whose main purpose is to perform precise vertex measurement. Around the silicon tracker is a multiwire drift chamber whose main purpose is to provide charged particle momentum measurement within the magnetic field of the CDF solenoid coil. The CDF magnetic field is provided by a 5-meter long superconducting solenoid coil. The magnet is operated to provide B field strength similar to Run I. The field strength has a central value of 1.41 Tesla and is uniform to 0.1% in the region $z < 150$ cm and $r < 150$ cm. The solenoid is built from Al-stabilized NbTi conductor with a maximum field strength of 1.5 Tesla and operating current of 5 KAmps at liquid-He temperatures of about 4.7K.

The silicon detector is composed of three subsystems; Layer 00 (L00), the Silicon Vertex Detector (SVXII), and the Intermediate Silicon Layer (ISL), as shown in Figure 8. All three systems use the same principle of silicon strip detectors - when a charged particle passes through the depletion region of a biased p-n semiconductor junction it creates electron-hole pairs which can be detected as electrical signals on a strip.

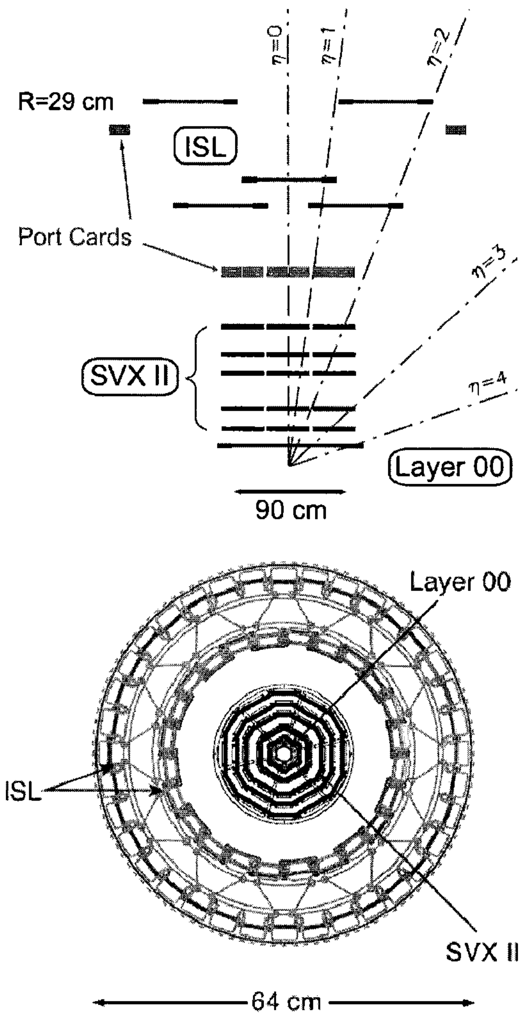

Figure 8. Silicon detector

L00 is the innermost layer of silicon tracker system. This single-sided, radiation-hard silicon sensor is placed immediately outside the beam pipe at a minimum radius of 1.35 cm. Inclusion of L00 in the tracking serves to improve the track impact parameter resolution.

SVX II is 90 cm long centered at the detector origin. It is composed of three 29 cm long cylindrical barrels. Each barrel is divided into 12 pieces (wedges) in azimuth with each wedge containing five layers of double-sided silicon micro strip detectors between radii of 2.4 cm and 10.7 cm. The outermost three layers combine an r - ϕ measurement on one side with 90° stereo measurement on the other. The innermost two layers of SVX combine r - ϕ information with small angle stereo at 1.2°. The stereo angle information from the layers is used to form a three-dimensional track. The silicon microstrips are supported by carbon fiber rails in assemblies called "ladders". Each ladder hosts four pieces of silicon sensors in two half-ladders. There are 12 ladders in ϕ and a total of 60 ladders in each barrel which are mounted between two beryllium bulkheads which also carry the water cooling lines for the readout electronics. The more than 400,000 channels in the system are connected to readout chips (SVX3) which reside on the surface of the silicon detectors. Each chip digitizes 128 channels. A parallel fiber optic-based data acquisition system reads out the entire detector in approximately 10 μs.

ISL consists of three separate silicon layers situated at radii of 20, 22 and 28 cm, respectively with respect to the beam line. Each layer is made up of double-sided micro strips as in SVX, only without the 90° stereo measurement. The ISL readout electronics are also similar to SVX, with the 30° wedge segmentation in readout being the same. ISL has more than 250,000 channels in readout.

The Central Outer Tracker (COT), as shown in Figure 9, is a 3m long cylindrically shaped drift chamber extending between $40 < r < 132$ cm. The COT has full coverage in the central ($|\eta| < 1$) region, and partial coverage in the forward region ($1 < |\eta| < 2$). It contains 8 “super-layers” each with 12 layers of sense wires interleaved with potential wires. Even-numbered layers are axial (parallel to the beam line), while odd-numbered layers are stereo ($\pm 2°$ from parallel to beam line). The COT is filled with a mixture of argon and ethane with small amounts of alcohol and oxygen. This gas mixture ionizes as a charged particle passes through it, leaving a trail of ions that drift toward the sense wires in the fields created by the potential wires. The ions avalanche close to the sense wire, producing a measurable electrical signal which is sent to the readout systems. A charged particle passing radially through the COT will give 96 measurements to which a track can be fit.

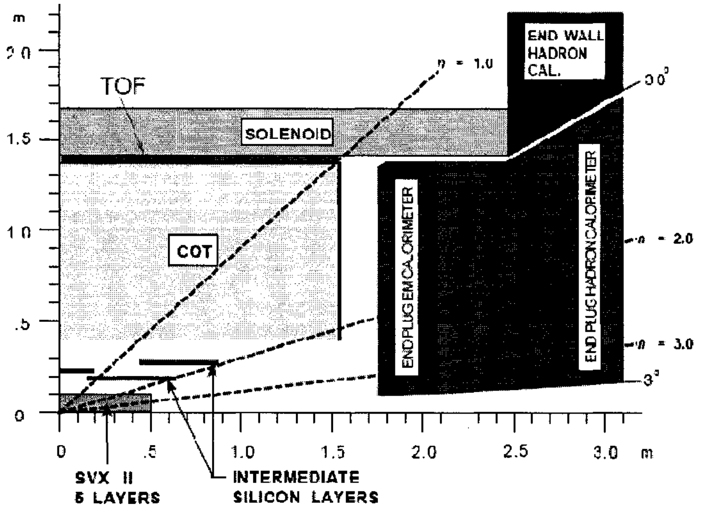

Figure 9. One quarter of the tracking system.

3.2.2 Time-Of-Flight Detector

The Time-of-Flight (TOF) detector system was installed during the CDF Run II upgrade. The main motivation for the TOF is to improve particle identification for flavor tagging. The TOF is located in the space between the COT and the solenoid cryostat, as shown in Fig.6, at a radius of 138 cm from the beam line. The system consists of 216 scintillation bars with dimensions of 4x4x279 cm. Each scintillator is read out by a photomultiplier tube (PMT) (Hamamatsu R7761) on each end, which provides time and pulse height measurements. Comparison of the results from each pair of PMTs gives the time and z coordinate information for the particle at the scintillator bar.

The time-of-flight, t, of the particle is defined to be difference between the arrival time at the TOF scintillator and the collision time t0. Similarly, the path length, L, of the particle is calculated in between the scintillator and the beam collision point. Using this information and the momentum of the particle, one can infer the mass of the particle. The time-of-flight resolution of the system is on the order of 100 ps. The matching of the scintillator information to a track is achieved by an extrapolation.

3.2.3 Calorimeters

Surrounding the CDF tracking volume (outside of the solenoid coil) are series of calorimeters. CDF uses scintillator sampling calorimeters, which provide a coverage up to about 3.64 units in $|\eta|$. In Run I, CDF calorimeters played an important role in the physics program by measuring electron, photon and jet energies. For Run II, the readout electronics for the central calorimeter system were upgraded. The forward region (endplug) went through a full upgrade and the previous (gas) calorimeter has been replaced by a new system to better accommodate the higher crossing rates for Run II. The CDF calorimeter system is a complex structure with four subdetectors to allow for maximum possible hermeticity. We describe each sub-detector below.

Central and End-Wall calorimeters: The central calorimeter is divided into two halves at $|\eta| = 0$ and each half consists of 24 wedges in azimuth. The central electromagnetic (CEM) calorimeter wedges consist of alternating layers of lead and polystyrene scintillator. The light signal is wavelength-shifted and carried by light guides to the PMTs (two per EM tower), which measure the number of scintillation photons produced in an EM shower that is formed during the particles' passage through the detector. To record the position of an EM shower, proportional chambers of wire and strips are embedded near the shower maximum (about 6 radiation lengths) deep into the EM calorimeter. The shower-track matching is performed using these chambers (CES), which helps electron, photon and pion identification and reduce fake electron rates. Another set of wire chambers is the preshower detector (CPR) which is located right in front of the CEM and uses the tracker and the solenoid coil as radiators. CPR is useful for pion-photon and electron separation.

The central and endwall hadronic calorimeters (CHA, WHA) use iron as the radiator and PMMA napthtalane scintillator. The endwall hadron calorimeter consists of modules mounted to the solenoid flux return to provide coverage from 30° to 45° on both east and west sides of the CDF detector. The hadronic segmentation and readout scheme matches that of the CEM.

Forward (End-plug) Calorimeter: The end-plug (plug) calorimeter is one of the major upgrade projects of CDF II. The old plug calorimeters, being gas-based, had a time response that would be incapable of matching the Run II Tevatron rates. The new plug calorimeter, which covers the $|\eta|$ region from 1.1 to 3.6 (polar angle from 37° to 3°), also matches better the segmentation and the projectivity of the central calorimeters. The calorimeter consists of EM and HAD parts, as is the case of its central counterpart. A section of the plug calorimeter is shown in Figure 10. The plug EM calorimeter is composed of 23 layers of lead/scintillator units. The first layer of units are used as a preshower detector (PPR) similar to CPR. As in the CEM, a shower-max detector (PES) exists in the plug calorimeter. The PES and PPR uses scintillating fibers read-out by multi-anode PMTs. The plug hadron calorimeter design aims at optimizing detector performance for various physics in the forward region. Similar to the EM section, it is composed of 23 layers, but of iron sandwiched scintillators.

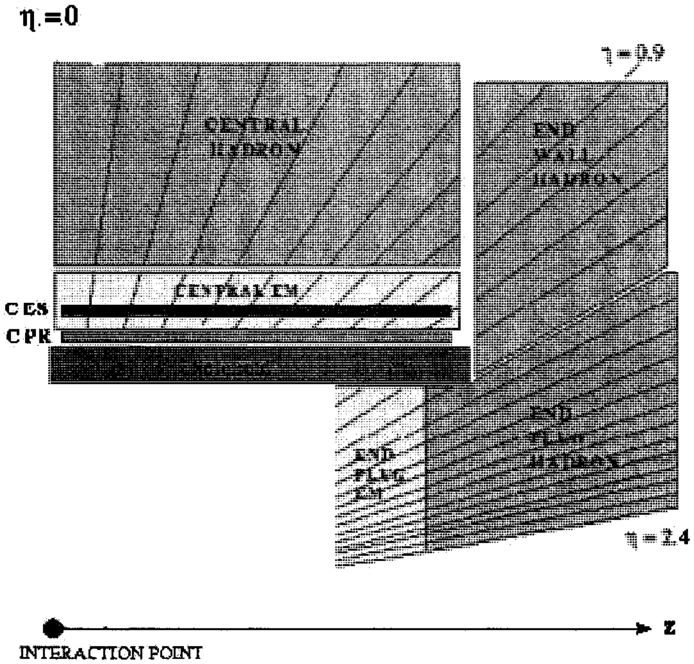

Figure 10. One quarter section of the plug calorimeter

3.2.4 Beam Shower Counters and Roman Pot

The Beam Shower Counters (BSC) [24] are used to trigger on diffractive events. They are made of scintillator paddles (read out with acrylic light-guides) wrapped around the beam line. There are 4 counters on the west side and 3 counters on the east, their position, geometry, and coverage are shown in Table 2 and Figure 11.

There are three Roman Pots along the beam pipe beyond BSC-4 on the west side, approximately 57m away from the interaction point. The purpose is to measure diffractive events. They are made of scintillator fibers, plus one scintillator tile per pot for triggers. Originally the Roman Pots were installed during Run I c, then retained for Run II. The Roman pots are equipped with bellows which allow them to move from their "out" position away from the beam pipe to their "in" position inside the beam pipe approximately 10mm away from the beam. Roman pot 1 is the closest to CDF detector and pot 3 is the farthest away.

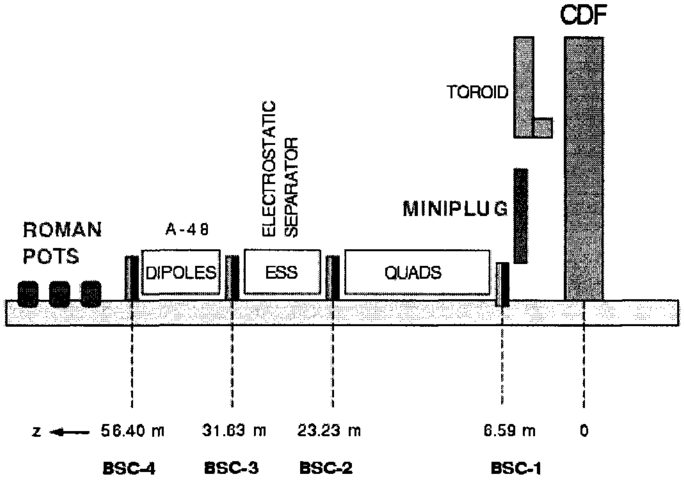

Figure 11. Beam Shower Counters

Counter	Z (m)	Inner R (cm)	Outer R (cm)	η coverage
BSC 1	± 6.6	3.8	5.9	$5.4 < \lvert\eta\rvert < 5.9$
BSC 2	± 23.2	3.8	7.6 (10.8)	$(6.1)\ 6.4 < \lvert\eta\rvert < 7.1$
BSC 3	± 31.6	3.8	7.6 (10.8)	$(6.7)\ 6.4 < \lvert\eta\rvert < 7.4$
BSC 4	56.4	3.8	7.6 (10.8)	$(7.0)\ 7.3 < \lvert\eta\rvert < 8.0$

Table 2. Geometry and Coverage of Beam Shower Counters

3.2.5 Cherenkov Luminosity Counter

The Cherenkov Luminosity Counter (CLC) is used to measure the instantaneous and integrated luminosity of the ppbar beam in the CDF detector. The CLC is located in the space between the plug calorimeter and the beam line, as shown in Figure 12. It is made of 48 aluminized mylar tubes (2m×2cm) filled with isobutane gas pointing toward the interaction point. The tubular construction makes the CLC very efficient to particles coming from the interaction point, but inefficient for particles coming from beam background and secondary interactions. This means that the CLC can efficiently count the number of bunch crossings with at least one ppbar interaction. Using this and the inelastic cross-section for pp interactions the luminosity can be determined.

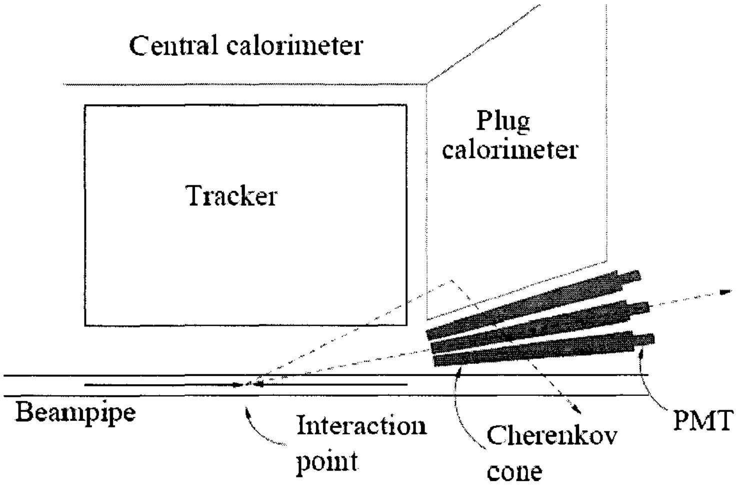

Figure 12. Cherenkov Luminosity Counter

3.2.6 Muon Chambers

The radially outermost component of CDF II is the muon system which consists of several sets of drift chambers and scintillators. There are 4 muon subsystems in CDF Run II: the Central Muon Detector (CMU), Central Muon Upgrade Detector (CMP), Central Muon Extension Detector (CMX) and Intermediate Muon Detector (IMU). The central part of the system is similar to Run I, except upgrades to improve readout and geometrical coverage. The IMU is new to Run II. The eta coverage of the muon system for Run II is shown in Figure 13.

The CMU detector is located right behind the central hadronic calorimeter at a radius of about 350 cm and has a cylindrically symmetric structure. The CMU is the first muon detector built for the CDF experiment. The calorimeters act as absorbers for almost all of the particles, except muons which do not shower as the electrons and photons. Figure 14 shows the location of one wedge of CMU chambers behind the CHA. Each wedge covers 12.6° and calorimeter towers cover 15°, so there exists a gap of 2.4° between wedges. Each CMU wedge consist of three modules (stacks) with four layers of 4 rectangular drift cells as shown in Figure 15. The cells have 50 μm sense wire at the center of the cell, running parallel to the z-xis. They are filled with Ar/Ethane (1:1) with some alcohol added.

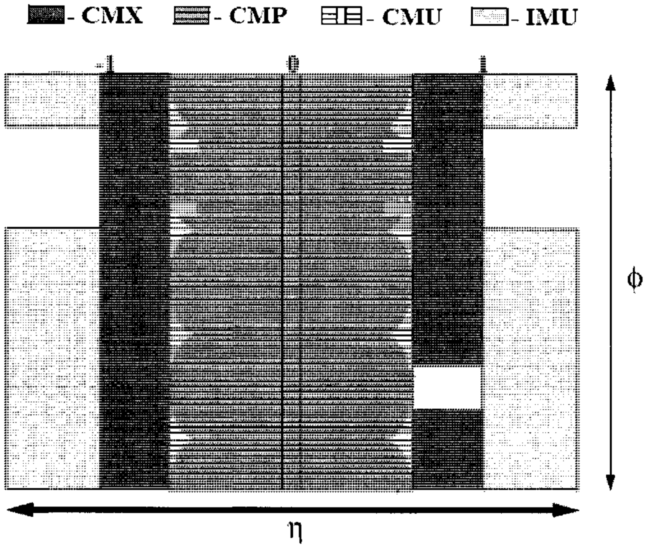

Figure 13. The eta coverage of the muon chambers

The CMP detectors were added during Run I to be mainly used in combination with CMU chambers to further improve the purity in muon identification. It forms a rectangular box around the detector and is located behind 60 cm steel. Due to the geometry of the detector, the η coverage varies with ϕ, as can be seen in Figure 13. The ϕ coverage of CMP was increased in Run II, with the addition of the section referred to as the "bluebeam". As in CMU, the CMP stacks consist of four layers of drift cells, but they are staggered by half cell per layer. The cells cannot provide information along the z-direction. On top of the outermost layer of CMP are the Central Scintillator Upgrade (CSP) system, consisting of a single layer of rectangular scintillator tiles.

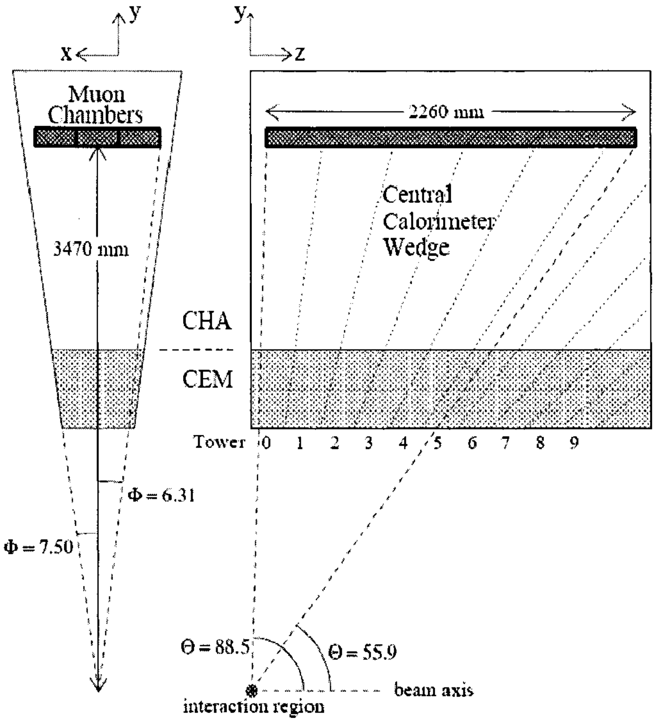

Figure 14. one wedge of the CMU chambers

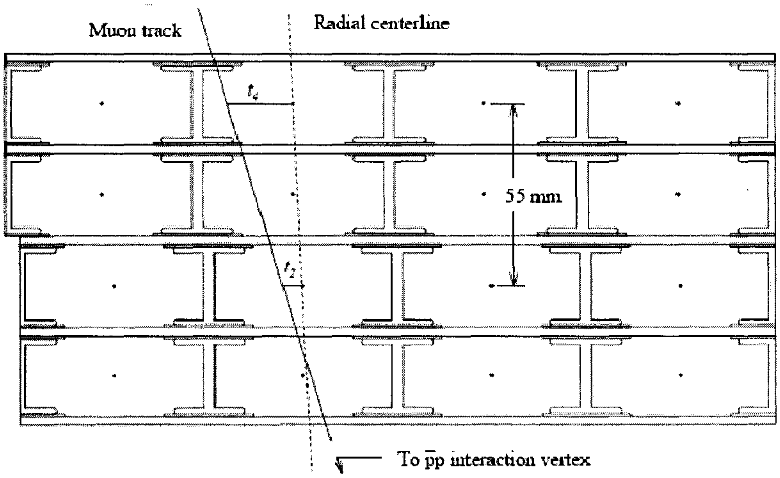

Figure 15. Four layers of 4 rectangular drift cells in one CMU stack.

The CMX is an extension to the CMU which started during Run I, to cover $0.6 < |\eta| < 1.0$. It is a conical arrangement of drift tubes similar to those of CMP cells and a sandwich of scintillators (CSX) system. The Run I CMX system, called the "arches" cover 240° in ϕ. The Run II upgrades for CMX includes the extension of ϕ coverage at the west top section (the "keystone") and the 90° gap at the bottom on both sides (the "miniskirts"). The east 30° gap at the top is filled with the instrumentation for the solenoid cryogenic system. The CMX detector layout is shown in Figure 16. The CMX segmentation in wedges is 15° in azimuthal angle. Each wedge has 8 layers of rectangular tubes in radial direction and 6 cells neighbor in each other in ϕ. The eight layers are grouped in pairs to form four continuous layers, each of which is half-staggered with respect to each other. The structure of CMX is given in Figure 17. The conical structure of CMX arches allows CMX z coordinate to be independent of phi on east and west sides of the CDF detector. This is not true for the miniskirt section, which has no curvature along its width. The CSX system consists of single layers of scintillator tiles on both sides of the CMX wedges in the arches. The miniskirt scintillation system (MSX) has only one layer of scintillator counters. The system is used in coincidence with the chambers to further improve the timing of the system and reduce the fake rates due to accidental muons (due to beam splashes, for example). In Run I, the pair of layers of CSX were used to time-in to the passing muon, in Run II, information from either of the layers is sufficient .

The IMU detector is a new system added to CDF detector at the beginning of Run II. It uses the toroid steel of old Forward Muon System to mount its chambers and scintillators. The toroid barrels are moved as close to the interaction region as possible to provide continuous muon detection in η. The upgrades in CDF tracker system and triggers make it possible to trigger and reconstruct IMU muons. The main parts of IMU are the chambers (BMU) and the scintillator layer (BSU) at the outermost radius of the toroid structure. The chambers are designed such that they are similar to those of CMU, both in readout and structure. There is also the Toroid Scintillator Upgrade (TSU) system which is made up of trapezoidal scintillators and is mounted in the inner face of the toroid, perpendicular to the beam line. IMU is expected to be prone to beam-related backgrounds at the rear end, where it is less shielded against the beam halo coming into the CDF interaction point.

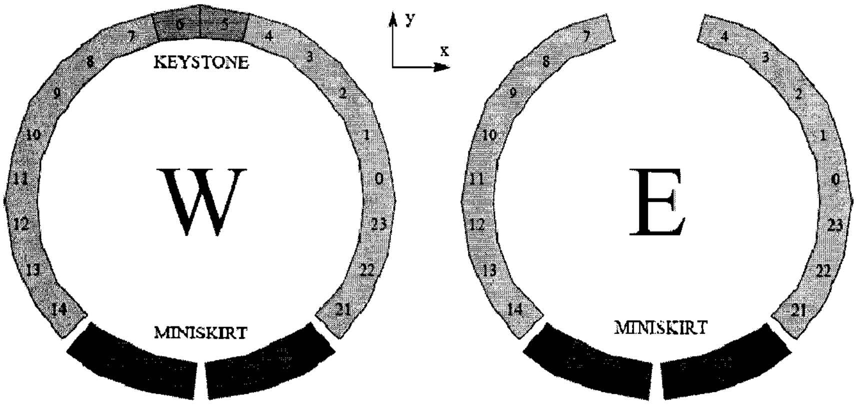

Figure 16. CMX detector layout

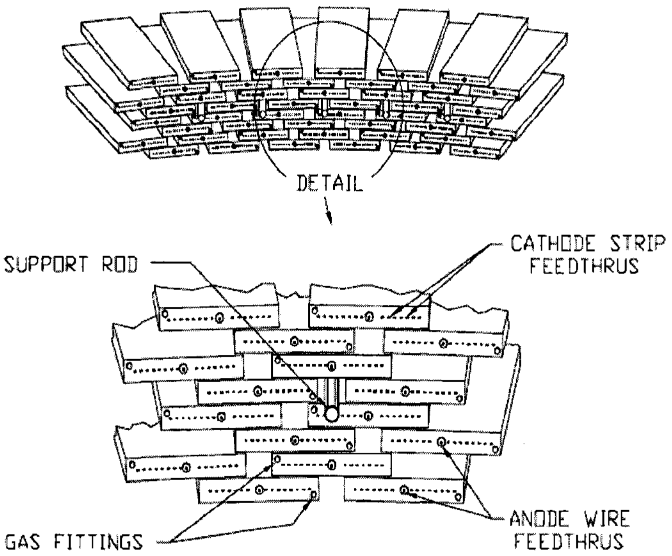

Figure 17. structure of CMX detector

3.2.7 Data Acquisition and Trigger System

The bunch crossing rate at CDF is as high as 2.5 MHz, it is impossible to record every event. A selection process is required to choose physically interesting events. CDF has a three level trigger system, each level putting more tight selection criteria on the events. It takes the 2.5 MHz bunch crossing rate down to 75 interesting events per second written to tape with only 5% dead-time. A detailed description of the trigger and data acquisition system can be found in Reference [25].

The Level 1 trigger takes the maximum bunch crossing rate of 2.5 MHz down to 30 kHz using hardware specifically designed for CDF. Information from the calorimeters, COT, BSC, and muon systems are processed into L1 calorimeter, track, and muon objects. To form a L1 calorimeter object, a 24×24 grid of trigger towers is formed by combining adjacent calorimeter towers into towers with $15° \times 0.2$ segmentation. The L1 calorimeter object is then defined as the EM or hadronic energy of the trigger tower. L1 track objects are 2-dimensional tracks ($pT > 1.5$ GeV/c) made by tracing COT hits with the eXtremely Fast Tracker (XFT) and extrapolated to the silicon region with the eXtremely fast exTRaPolator (XTRP). L1 muon objects are composed of muon chamber stubs being matched to tracks from the XTRP. All these L1 objects are sent to the "Global L1" processing, where they are combined with logical AND and OR gates to form L1 trigger decisions. "Global L1" has capacity for 64 different L1 triggers.

The Level 2 trigger is also made of custom built hardware and takes the 30 kHz L1 rate and reduces it to 350 Hz. L2 decision is made within all the information from L1, plus information from the SVX and CES. L2 calorimeter objects use an elementary clustering algorithm. A cluster is defined as a contiguous region of L1 trigger towers with non-trivial energy. Each cluster begins with a tower above the seed threshold, then all towers above a shoulder threshold that form a contiguous region with the seed tower are added to the cluster.

All L1 and L2 decisions are temporally coordinated with the Trigger System Interface and Clock (TSI/CLK). The Level-3 (L3) trigger is a farm of ~500 CPUs in PCs running Scientific Linux. It does a full event reconstruction for every event coming from L2. It takes roughly 1 second for a CPU to process one event. Having full event reconstruction at L3 means that event selection is very flexible and can be very specific with fully reconstructed tracks and jets. L3 takes the 350 Hz input from L2 and outputs events at 75 Hz. It's a mean event size of ~200kB, which is 15 MB/s being written to tape.

3.3 Muon Detection at CDF

In this section, the muon detection and identification is briefly described. CDF detector uses a collection of single-wire, gaseous drift chambers and organic scintillator tiles for muon detection and triggering, as briefly introduced in previous sections. In the following sections, we outline the basics of drift chambers, readout, trigger and reconstruction and identification. An detailed description of the methods in this section can be found in Reference [26] and [27].

3.3.1 Muon Detection Techniques

A drift chamber is a type of gas chamber detector which is based on direct collection of the ionization of electrons and ions produced in a gas by a passing charged particle. A single-wire drift chamber with a rectangular cross section is shown in Figure 18. A penetrating muon ionizes gas inside the chamber with negligible energy loss. The chamber sustains a net positive voltage difference between the anode (sense) wire and the cathode (field) plates. The positively charged ions drift toward the cathode field, the ionization electrons drift toward the anode wire. The electrons create an avalanche of charge as they come nearest to the wire and produce a pulse as the charge hits in the wire. The pulse is sent to the readout electronics and collected as signal. The distance, D, of the muon to the wire is measured using the drift time of the pulse and the drift velocity, Vd. The drift velocity of a chamber is dependent on the grid voltage (uniform) and the gas content. CDF muon uses Ar/C_2H_6 bubbled through isopropyl alcohol. Argon is a noble gas. Ethane (C_2H_6) is the quencher. The role of a quencher is to absorb photons emitted from Ar, through vibrational and rotational degrees of freedom. It also helps tune drift velocity and signal gain. It has been shown that the usage of alcohol, as the additive vapor, helps as a quenching agent to prevent breakdowns, glow discharges and aging. Most drift chambers employ a field shaping to get almost a constant drift velocity across the chamber. The details of the voltage grid of the CMP and CMX chambers can be found in Reference [26]. In CMU detector, the neighboring chamber are ganged together such that the relative amounts of charges collected in the resistive anode wires can be used to measure the position of the muon along the wire (z). Similar measurement can also be performed for the BMU detector.

Operating gaseous chambers is a difficult task. The most common problem in operating chambers is the breakdown process. A breakdown occurs when the voltage across the cathode and anode gap drops by a process which produces a high conductivity between cathode and anode [28]. The mechanisms of breakdown in wire chambers are usually related to the chemical reactions of the particles, such as electrons, ions, molecules and photons, within the chamber plasma and with their interactions with the cathode. It has been especially observed that when ultraviolet photons from excitations of the gaseous medium are not completely quenched. Self-sustaining discharges often occur for the gaseous chambers, such as "sparks" which are complete breakdowns of inter-electrode gap. "Glow discharges" occur when self-sustained currents develop and dark-current rates increase. Under sustained irradiation wire chambers can "age", which is a degradation of operating characteristics, commonly as a result of formation of deposits of molecules on the anode wires or cathode plates changing the gain of the chamber.

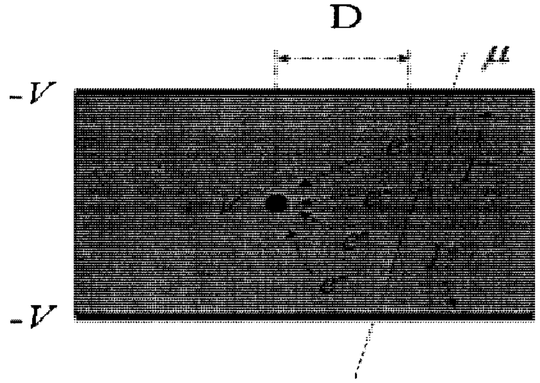

Figure 18. A single-wire drift chamber, a rectangular cross section view

3.3.2 Muon Trigger

The muon detector information can be triggered on Level 1 of CDF triggering system. The muon stub information is obtained in bitwise information in the transverse momentum of the particle that is passing through it. Arrangement of the anode (sense) wires within a muon chamber permits a lower bound on the P_T of a particle to be determined [29]. The angle between a particle track and the radial line passing through the anode wires can be determined by measuring the difference in arrival times of the drift electrons (Δ_t). A further relationship can be derived between this angle and the angle of deflection due to the magnetic field surrounding the tracker, which is in turn related to the P_T of the passing muon track. Therefore, a crude measurement of the muon P_T can be performed by using the Δ_t information. This relation is derived for the CMU chambers, but in principle, may be applied to all the muon detectors. Figure 19 shows the trigger-pair of the CMX system. The trigger-pair chambers are selected to be the the pair of chambers that lie at the same phi. If the drift time difference between a trigger pair is < 124 ns, the L1 muon "primitive" trigger fires a "High P_T stub", if it is less than 396 ns (beam crossing time), then it is a "Low P_T stub". For the CMX and IMU systems the scintillator information is also attached to the trigger. The CMP detector information is obtained through a specific pattern finding using four layers of drift tubes. The IMU system also makes use of the HAD calorimeter timing information to further bring down the trigger rates down. Figure 20 shows the diagram of the Level 1 muon trigger in Run II. The high P_T muon track identification in the COT is accomplished in the XFT processor at Level 1, as discussed in previous sections. The information of the track trigger (XTRP) and the muon stub information are matched in the “Muon Matchbox card” over an entire 30° azimuthal wedge of the CDF detector, the matching is performed in r-phi plane only, not 3D. From then on, the information can be passed to the Level 2 trigger.

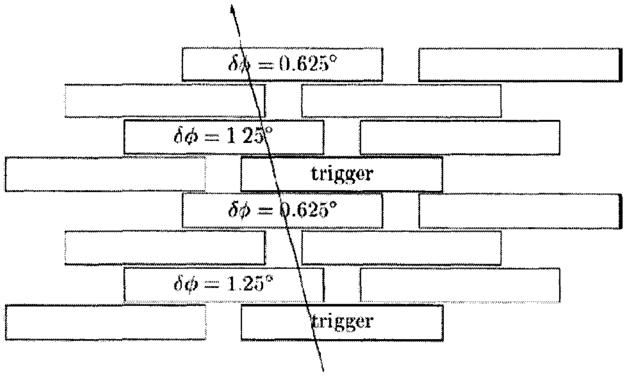

Figure 19. A trigger-pair of the CMX system

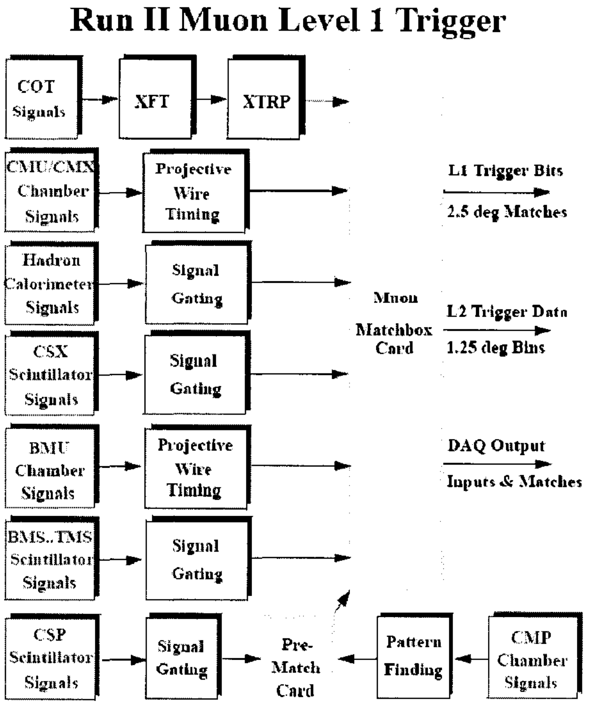

Figure 20. Diagram of the Level 1 muon trigger in Run II

3.3.3 Muon Reconstruction

The data that are collected by the trigger need to be reconstructed with the CDF offline software, with very loose reconstruction requirements and with the calibrations and corrections applied. The common calibrations include the global alignment of the detectors with respect to the central tracker and the drift velocities for a correct measurement of drift distances.

The passage of a muon in CDF detector and the CMU and CMP chambers is shown schematically in Figure 21. The muon track parameters are measured in the tracking volume and the 4-momentum of a "CDFMuon" comes from its track. The calorimeters act like absorbers and they give the measure of the EM and HAD energies. The muon then passes through the muon chambers (in this case CMU and CMP), such that muon chamber tracking (forming "stubs") can later on be performed. A muon stub is formed using the hit information and stub finding and fitting algorithms for the sub detectors. The output of the fits is the stub position and direction vectors [27]. A muon stub is required to have at least 3 hits associated to it.

The muon track helices are parameterized at the point of closest approach to the origin in x - y (i.e. r-ϕ) plane of the CDF detector [30]. The axial (r-ϕ) parameters are the impact parameter (d_0), azimuthal angle (ϕ_0), and the curvature (P_T). The stereo (r-z) parameters are the z position (z_0) and the cotθ, of the angle with respect to the z-axis at the point of origin. The cot$\theta$is defined as P_Z /P_T. The curvature is defined as c=1/(2R) where R is the radius of the curvature of the track. For a negatively charged particle, the curvature has a negative sign. The relation between P_T and curvature is:

$$p_T = \frac{B}{2 \cdot c_l} \times \frac{1}{c} = \frac{0.002117}{c}$$

where c_l is the speed of the light. For a tracking volume of fixed magnetic field, P_T is only a function of c (or R).

If the tracks use only the COT information, they are usually "beam-constrained" (BC) at the analysis level, since they are reconstructed with respect to the z-axis of the CDF detector. This is performed refitting the track by using the measured position of the beam line. This procedure improves the momentum resolution of the tracks.

The muon tracking stops at the face of the COT. From then on, a procedure should be applied to match a stub candidate in the muon chambers to the muon track candidate. Also the path of the muon inside the calorimeters is not measured. Therefore, "extrapolations" are used to extrapolate the track to the stub. The measure of this quantity in r-ϕ plane, usually called Δx, is one of the basic criteria for selecting a muon candidate in CDF detector (Section 4). Table 3 summarizes the criteria for reconstructing a CDFMuon in the CDF offline code.

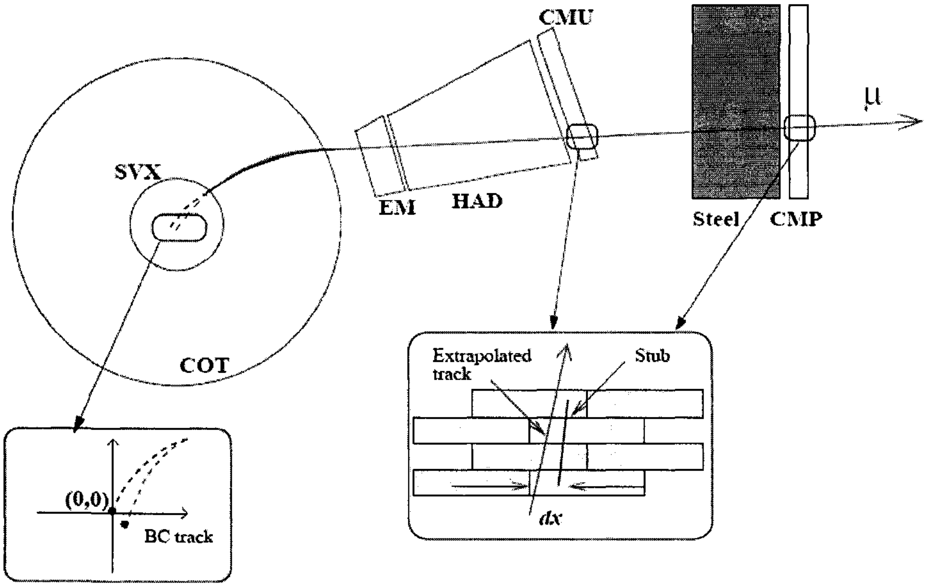

Figure 21. The passage of a muon in CDF detector

Parameter	Criteria
pT	> 1.3 GeV/c > 10 GeV/c (stubless)
$\lvert Z_0 \rvert$, $\lvert d_0 \rvert$	< 200 cm, < 6 cm
Track hits in COT (N_{axial})	>= 10
$\lvert \Delta x \rvert$	< 30 cm (CMU) < 60 cm (CMP) < 50 cm (CMX) < 90 cm (BMU)
$\lvert \Delta z \rvert$	< 250 cm (CMU) < 330 cm (CMP) [325 cm, 550 cm] (CMX) [440 cm, 840 cm] (BMU)

Table 3. criteria for reconstructing a CDFMuon in the CDF offline code

4. Cross Section Measurements

4.1 Data and Event Selection

Selecting potentially interesting events from the 2 million bunch crossings per second is achieved with a trigger to write the events to tape. The triggered events are then passed through offline reconstruction and stored on tape. We utilize the Stntuple (a kind of ntuple data format) data sets: gdifah, gdifai and gdifaj, covering run period 1-11, corresponding to run 190697 - 237795. The reconstructed events are passed though a sequence of offline cuts to select interesting events from those on tape. The offline cuts include: acceptance cuts; muon quality cuts; exclusivity cuts and cosmic veto cuts.

4.1.1 Trigger and good run list

A good run list is applied to the dataset to eliminate runs in which a detector component was not functioning properly. In this analysis we are using a good run list (covering the period 1 to 11, provided by Data Quality Monitoring group, Version 17) that requires CMU, CMP, CMX and COT are functioning properly. The total luminosity corresponding to those good runs is 1484 pb^{-1}. The name of the trigger employed is "DIFF_CHIC_CMU1.5_PT1.5_TRK". At Level 1 the trigger requires one CMU muon with $P_T > 1.5$ GeV/c and a gap in both east and west BSC. Level 2 is auto-accept. At Level 3 a muon and an additional track are required where the invariant mass of this pair is in the range 2.7 GeV/c^2 < M(muon+track) < 4.0 GeV/c^2. The trigger details are summarized in Table 1.

4.1.2 Acceptance and muon quality cuts

The initial offline cut employed was the selection of those events with two reconstructed muons (also named TStnMuons). A set of muon quality cuts, as listed below, is then applied to both muons to further select good muons. The muon quality cuts are based on the standard low P_T muon offline cuts at CDF [31]-[34].

- **$D_0 < 1$ cm**
- **$Z_0 < 60$ cm**
- **NCotAxSeg(5) ≥ 3**
- **NCotStSeg(5) ≥ 3**
- **HasCmuStub == true**
- **CmuDelX < 12.0 cm**
- **CmuChi2 Link < 3**
- **EmEnergy < 1.0 GeV**
- **HadEnergy < 4.0 GeV**
- **CalEnergy (Em+Had) > 0**

Where D_0 is the impact parameter (perpendicular distance, in 3D, from the interaction point to the muon track); Z_0 is the distance, alone z-axis, between the interaction point and the muon track; NCotAxSeg(5) is the number of 5-hit axial stubs in the COT; NCotStSeg(5) is the number of 5-hit stereo stubs in the COT; HasCmuStub means there exists reconstructed stubs in the CMU; CmuDelX is the distance between the CMU stub and the extrapolated COT track; CmuChi2Link is the χ^2 of the fit of CMU stub; Em (Had) Energy is the energy deposited in the electromagnetic (hadronic) calorimeter.

4.1.3 Cosmic veto cuts

In order to remove cosmic muons from the data we use the Time Of Flight (TOF) information. The difference between the TOF of the two muons is required to be less than 3 ns. However, a significant number of the muon pairs do not have a valid associated TOF. Thus, one cannot get a correct value for the TOF difference. For those events we utilize the 3D opening angle instead to veto cosmic muons, requiring a 3D opening angle of less than 3.0 radians. A plot of the time difference between the hits in TOF of the two muons is shown in Figure 22. A scatter plot of the time measured in the TOF counters for both muons is also given in Figure 22, the faint band denoting the cosmic ray events. Lastly, Figure 23 shows the distribution of the 3D opening angle between the two muons of those events that do not have valid TOF information, the small peak at ~3.1 radians is due to the comsic ray contamination. Table 4 summarizes the cosmic veto cuts.

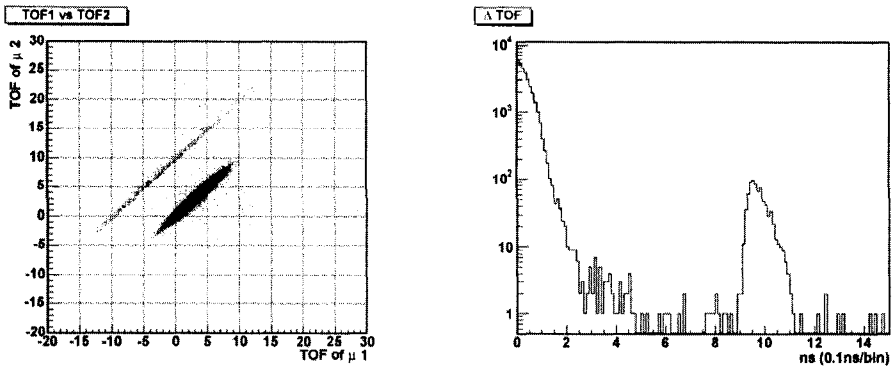

Figure 22: Scatter plot of the times each muon hit the TOF, for each pair of muons in ns (left), and the time difference between the muon hits in the TOF in ns (right) for events that have valid TOF information.

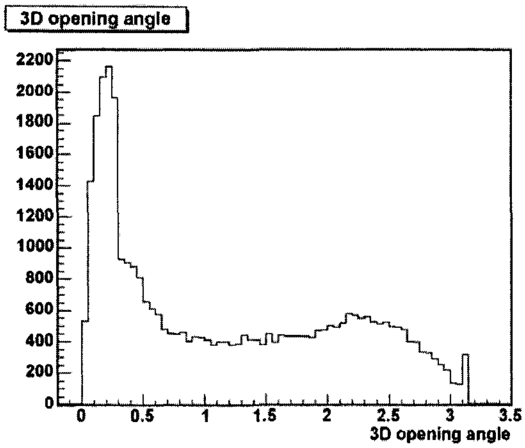

Figure 23: The 3D opening angle of the muon pair in radians for all muon-pair events that do not have valid TOF information.

	Cosmic Veto cut
Both Valid TOF = true	**ΔTOF < 3 ns**
Both Valid TOF = false	**3D open angle < 3.0**

Table 4. Summary of Cosmic Veto cuts

4.1.4 Exclusivity cuts

In order to determine if the event was exclusive, one must determine that there was nothing (other than the two EM objects) in the detector. In order to do that, you must know what "nothing" looks like in the detector. To accomplish this, two samples of events were made from zerobias data, *interaction* and *non-interaction*. Events with no tracks (above the default CDF track of $P_T = 200$ MeV/c), no hits in the CLC (a hit defined as >150 ADC counts), and no muon stubs, were put into the non-interaction sample, all others were put into the interaction sample. In the remainder of this section these samples will be used to motivate the exclusivity cuts on the Beam Shower Counter (BSC) and calorimeters. Note that the no track, CLC, and muon cuts are not being applied to the exclusive electron sample, they are only being use to help define appropriate calorimeter cuts that will be applied to the signal sample.

Figure 24 shows the maximum number of ADC counts in any of the BSC-1 PMTs for the interaction and non-interaction samples (one entry per event) in Run II period 9. It shows that a cut of 500 ADC counts separates interaction and no interaction data in BSC1. Thus, an event must have all BSC-1 channels less than 500 counts to be defined as exclusive. Figures 24 also shows the corresponding plots for BSC2 and BSC-3, where the exclusivity cuts are 300 ADC counts and 500 ADC counts, respectively.

The calorimeters are divided into five regions; mini-plug region (towers 22 to 25 $3.6 < |\eta| < 5.2$), the forward-plug region (towers 18 to 21 $2.11 < |\eta| < 3.64$), the mid-plug region (towers 12 to 17 $1.32 < |\eta| < 2.11$), and the end-wall region (towers 6 to 11 $0.66 < |\eta| < 1.32$), and the central region (towers 0 to 5 $0.00 < |\eta| < 0.66$). Using running period 9 as an example, Figure 25 shows the highest E_T tower for the five regions in the interaction and non-interaction samples. The central and end-wall regions are divided into EM tower and HAD tower cuts due to the large difference in the noise levels of the two sections. These plots motivate the cuts shown in Table 5.

The exclusivity cuts are applied to all towers in two-candidate events except for the muon towers. A muon tower is defined as any tower in the CdfEmObject's

TowerLinkList (defined in Stntuple offline code) plus any towers within $\Delta R < 0.3$, where $\Delta R \equiv \sqrt{\Delta\eta^2 + \Delta\phi^2}$.

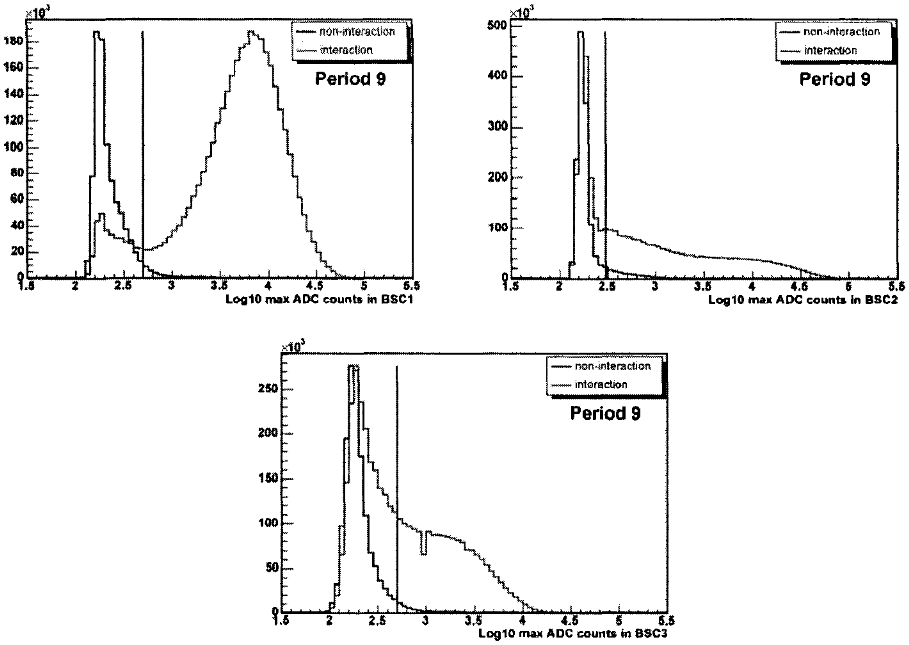

Figure 24: Log10 (ADC counts - pedestal) in BSC-1, BSC-2 and BSC-3 for interaction and non-interaction samples, the line shows the cut values.

Region	Towers	Eta Range	Cut
BSC-3	n/a	$6.7 < \lvert\eta\rvert < 7.4$	< 500 ADC counts
BSC-2	n/a	$6.4 < \lvert\eta\rvert < 7.1$	< 300 ADC counts
BSC-1	n/a	$5.4 < \lvert\eta\rvert < 5.9$	< 500 ADC counts
Mini Plug	22 to 25	$3.6 < \lvert\eta\rvert < 5.2$	ET < 3 MeV
Forward Plug	18 to 21	$2.11 < \lvert\eta\rvert < 3.64$	ET < 30 MeV
Mid Plug	12 to 17	$1.32 < \lvert\eta\rvert < 2.11$	ET < 80 MeV
End Wall	6 to 11	$0.66 < \lvert\eta\rvert < 1.32$	EM E_T < 80 MeV, HAD E_T < 200 MeV
Central	0 to 5	$0.00 < \lvert\eta\rvert < 0.66$	EM E_T < 80 MeV, HAD E_T < 200 MeV

Table 5: Summary of exclusivity cuts

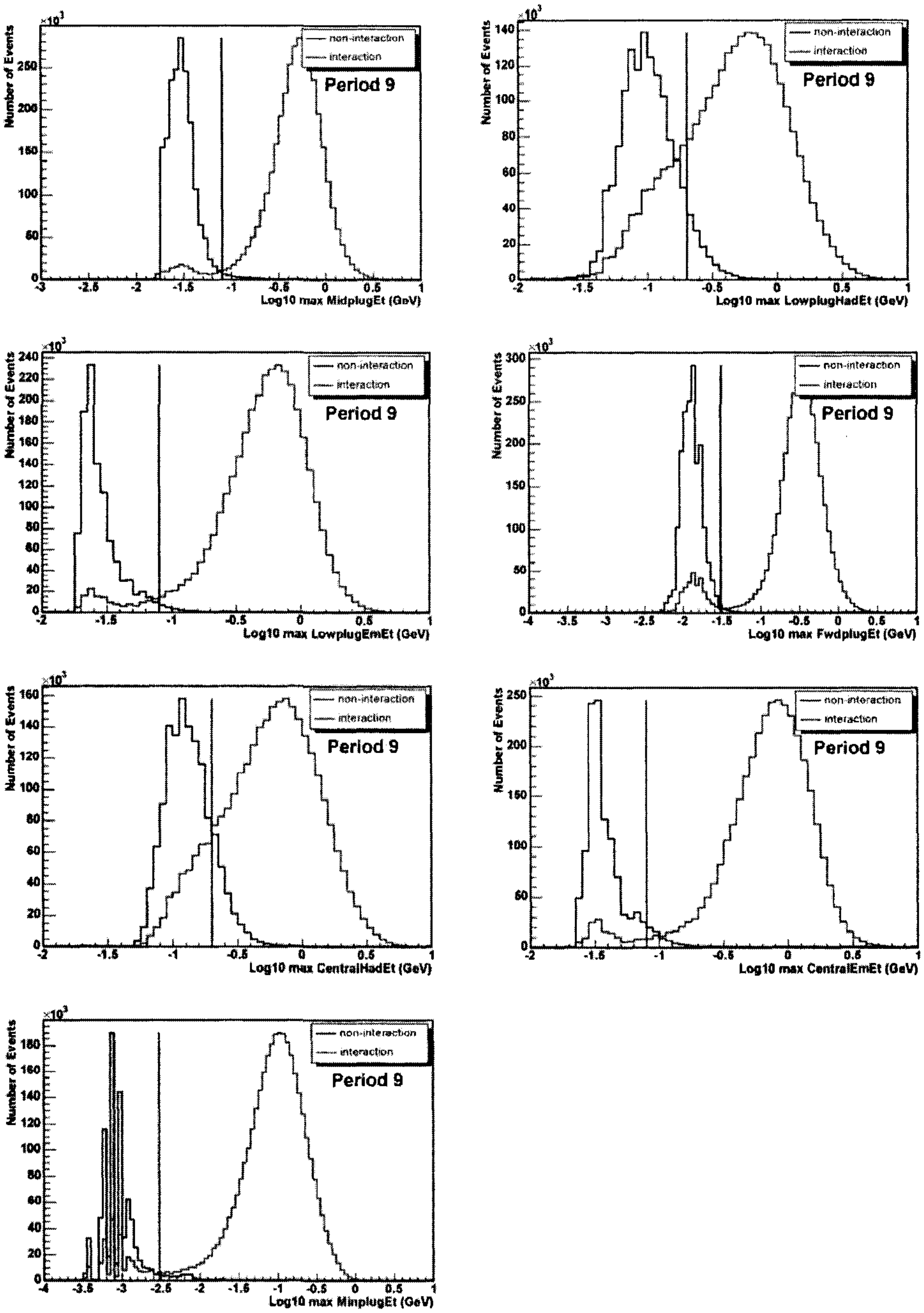

Figure 25: Log10 (Max Et) for Central, End-wall, Mid-plug, Forward-plug, Mini-plug regions, for interaction and non-interaction samples, the lines show the values of exclusivity cuts.

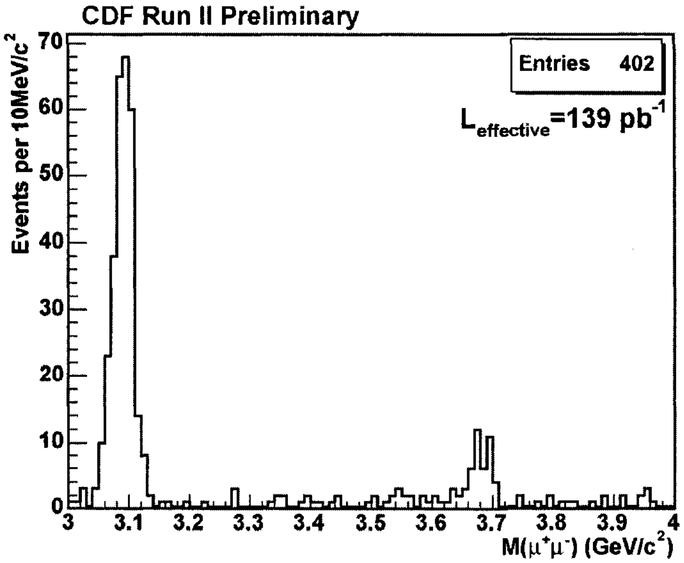

Figure 26: The invariant mass distribution of the exclusive muon-pair sample. The peaks corresponding to the J/ψ and ψ' vector mesons states can be clearly seen, along with continuum muon-pair production via two-photon interactions.

4.1.5 Signal events compared with Monte Carlo events

After the muon quality cuts, cosmic veto cuts and exclusivity cuts we finally found 402 events exclusive dimuon events from period 1-11 data, as shown in Figure 26. Those events arise from three sources: continuum contribution of two-photon production ($\gamma\gamma \rightarrow \mu^+\mu^-$); photoproduction of J/ψ and ψ' that subsequently decay into muon pairs; and $J/\psi \rightarrow \mu^+\mu^-$ from the χ_C decay, where the soft photon is missed (survived the exclusivity cuts). The signal events are divided into three mass windows and compared with STARLIGHT MC events. The MC events have been passed through detector simulation, offline muon reconstruction and muon quality cuts. The MC events experienced all major losses as signal events, so they are comparable with the signal events. Figure 27, 28 and 29 show good agreement between signal events and MC.

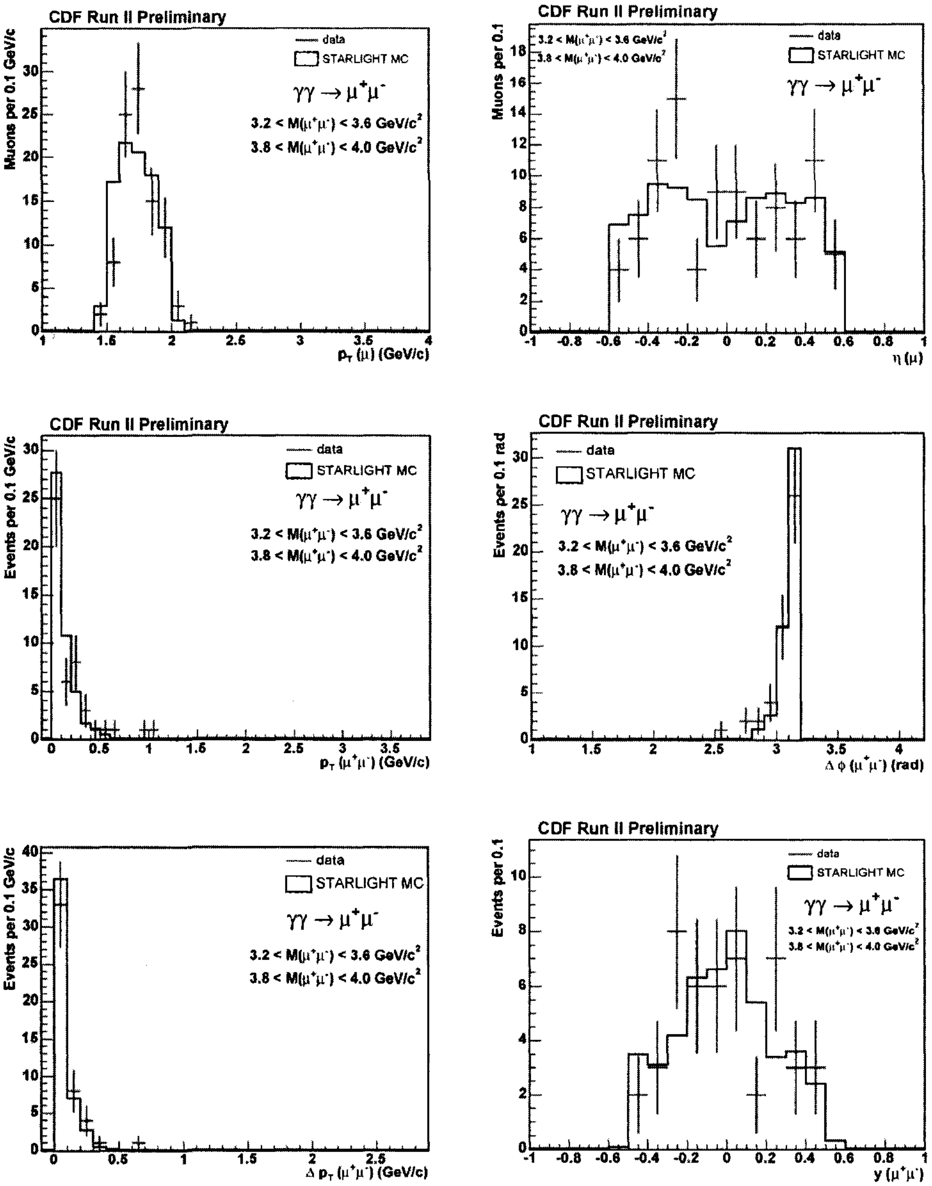

Figure 27: The kinematic distributions for QED continuum μ+μ− production (data events in mass window: [3.2, 3.6]+[3.8,4.0]) compared with the STARLIGHT MC events.

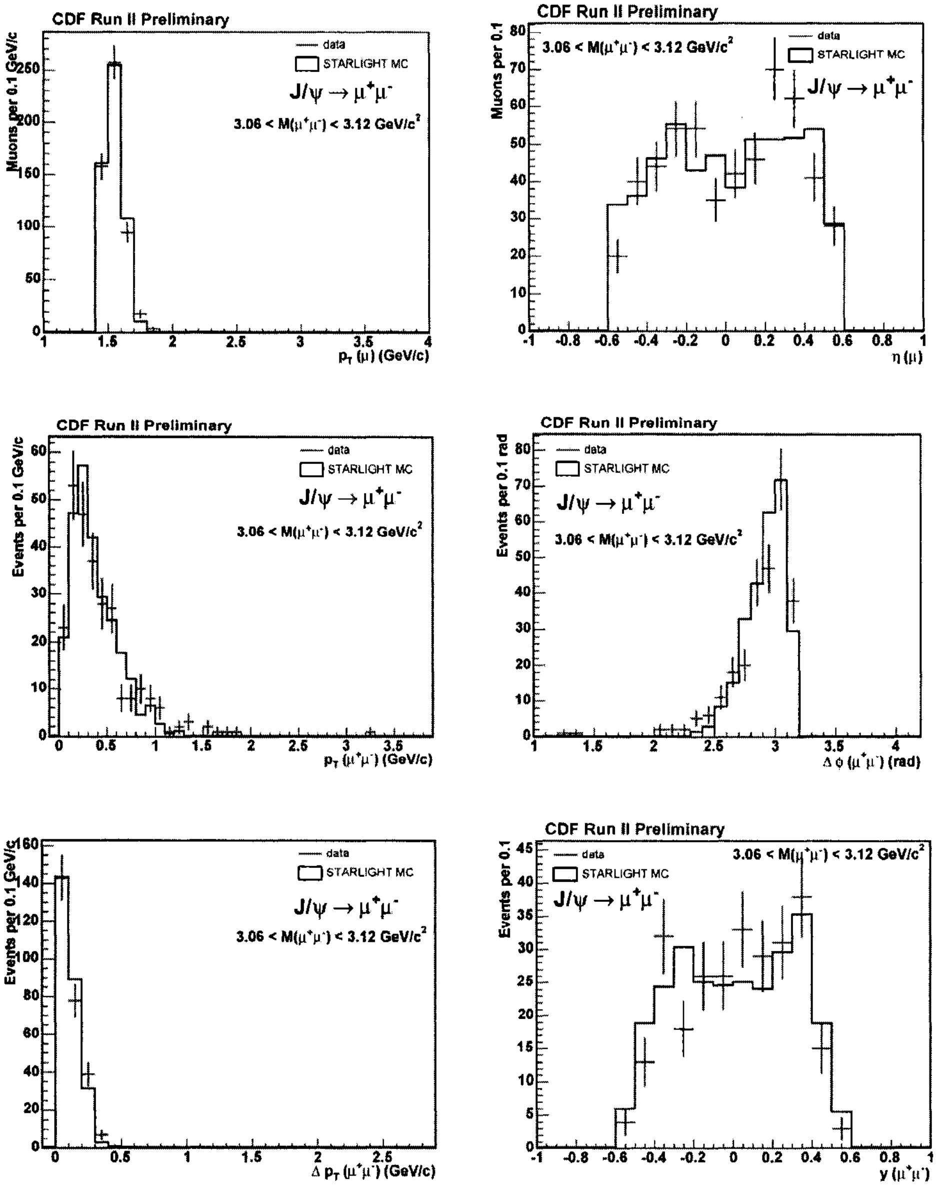

Figure 28: The kinematic distributions for $J/\psi \to \mu^+\mu^-$ photoproduction (data events in mass window: [3.06, 3.12]) compared with the STARLIGHT MC events.

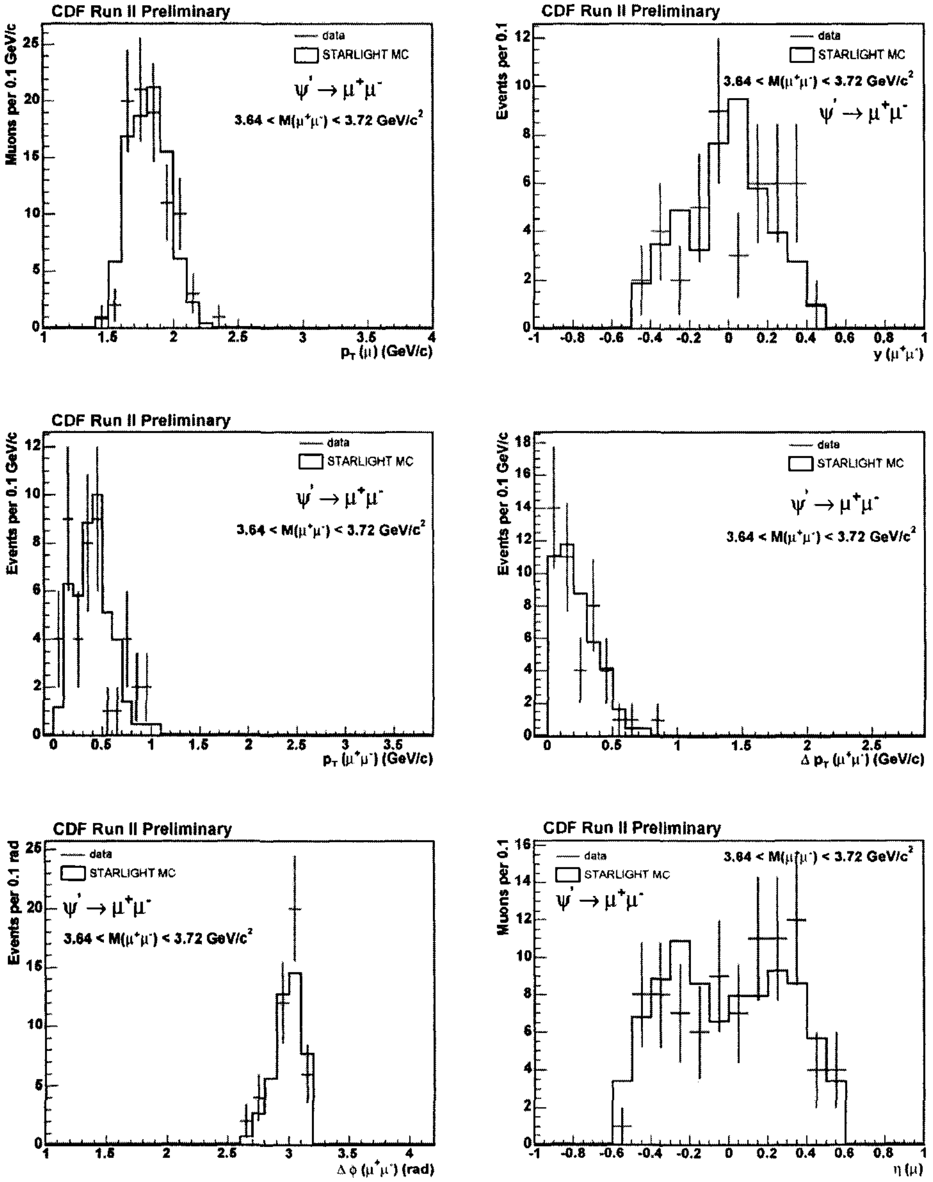

Figure 29: The kinematic distributions for $\psi' \to \mu^+\mu^-$ production (data events in mass window: [3.64, 3.72]) compared with the STARLIGHT MC events.

4.2 Efficiencies

In order to calculate the cross-sections, the observed number of signal events should be corrected by the efficiency for each of those steps where signal events could be lost:

- The geometric and kinematic region where we used to search for signal events refers to **Acceptance (A)**. It's the number of events that fall into $|\eta_{\text{each }\mu}| \leq 0.6$, $P_{T_{\text{each }\mu}} \geq 1.4\ \text{GeV/c}$ and $3.0 \leq \text{mass} \leq 4.0\ \text{GeV/c}^2$ divided by the total number of events that occurred at the interaction point (covering whole 4π solid angle and P_T goes from 0 to ∞).
- Some muon-pair candidates are lost because of the limited kinematic and geometric coverage of the detector, for example the cracks between muon towers in CMU and the inefficiency of CMU to find all P_T>1.4 GeV/c muons. This part of loss refers to **Detector Efficiency**. To determine this efficiency we put a sample of MC events (that fall inside Acceptance) through the detector simulation program, and count the fraction that survived.
- The number of candidate events for which the trigger successfully fired as a fraction of the total number of candidates that should fire the trigger is called the **Trigger Efficiency (ε_{L1})**.
- Triggered events are passed to offline reconstruction. The fraction of triggered candidates that are successfully reconstructed offline is called the offline **Reconstruction Efficiency**.

  In practice the reconstruction process is combined together with detector simulation program (mcProduction 6.1.4 is used in this analysis). So we will present one number for "**Detector Efficiency × Reconstruction Efficiency**" (**$\varepsilon_{\text{det.rec}}$**) rather than two separate numbers.
- After offline reconstruction, the events are analyzed (Stntuple in this analysis), the initial stage of analysis involves the use of muon quality cuts and cosmic veto

cuts, each with their respective, **Quality Cuts Efficiency (ε_Q)** and **Cosmic Veto Efficiency**.

- Finally, we have the exclusivity cuts and their corresponding **Exclusive Efficiency (ε_{exc})**

Since an inelastic p$\bar{\text{p}}$ interaction on top of an exclusive interaction in a beam crossing will make the exclusive interaction unobservable, the exclusive efficiency is highly dependent on instantaneous luminosity. Accounting for exclusive efficiency in the cross section is done with a quantity called the **Effective Luminosity (L_{effe})**.

4.2.1 Detector Efficiency and Reconstruction Efficiency

We use muon-pair events generated with the STARLIGHT MC as a representative sample of exclusive dimuon events. The events are then passed through the mcProduction version 6.1.4 (which includes both CDFSim and offline muon reconstruction) to simulate the effect of the process in the CDF detector. By counting the number of events that survived the detector simulation and offline reconstruction, we get an estimate of the detector efficiency with reconstruction efficiency.

The convolution of the detector efficiency with the reconstruction efficiency as function of muon-pair mass, P_T and true rapidity as calculated using the STARLIGHT MC with mcProduction is shown in Figure 30, where the data for the J/ψ, ψ' and the QED continuum are shown separately. The convolution of the detector efficiency with the reconstruction efficiency as function of each muon η and ϕ and P_T is shown in Figure 31. Table 6 summarizes the overall Detector Efficiency × Reconstruction Efficiency.

	$\varepsilon_{\text{det.rec}}$
$\gamma\gamma \rightarrow \mu\mu$	**41.76 ± 1.50 %**
$J/\Psi \rightarrow \mu\mu$	**18.83 ± 0.27 %**
$\Psi' \rightarrow \mu\mu$	**53.92 ± 2.78 %**

Table 6. Summary of overall Detector Efficiency × Reconstruction Efficiency

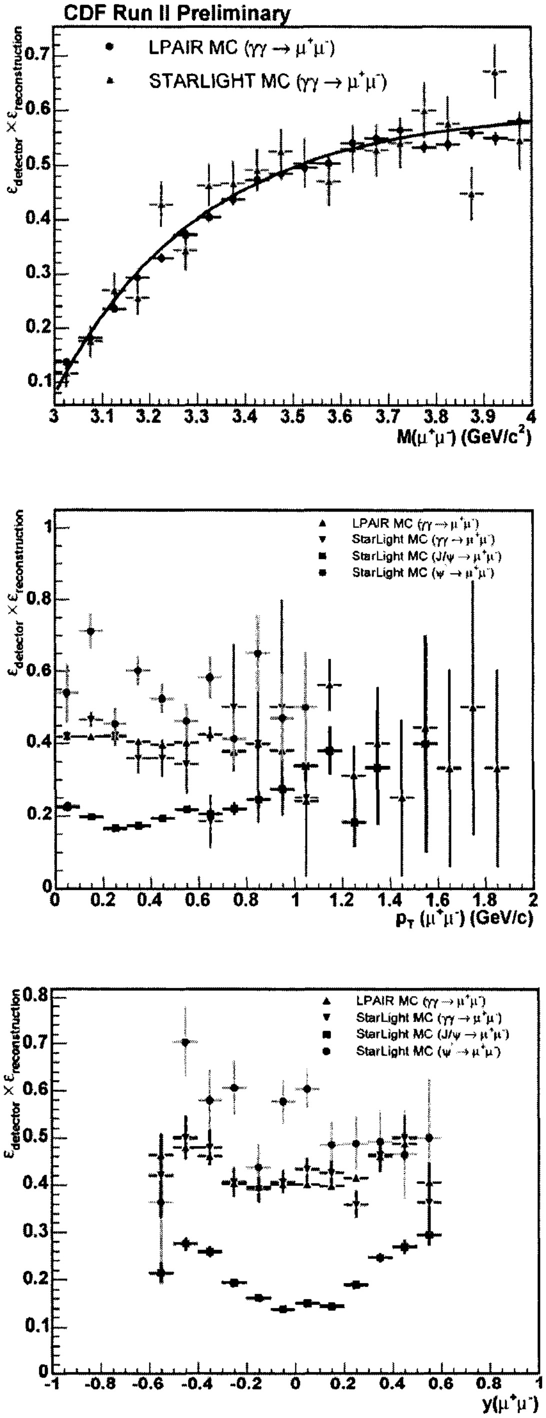

Figure 30: The convolution of $\varepsilon_{\text{det.rec}}$ as function of muon-pair mass (top), P_T (middle) and true rapidity (bottom) as calculated using the STARLIGHT MC and mcProduction 6.1.4.

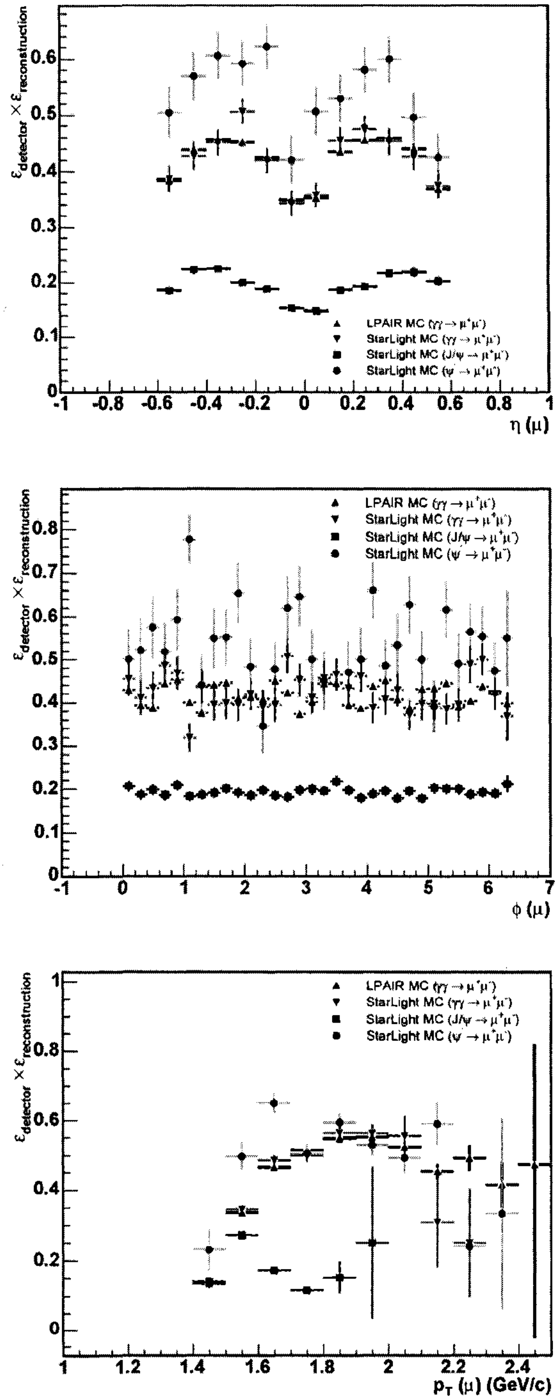

Figure 31: The convolution of the $\varepsilon_{det.rec}$ as function of muon P_T (top), η (left), ϕ(right) as calculated using the STARLIGHT MC and mcProduction 6.1.4

4.2.2 Trigger Efficiency

The trigger efficiency of the "DIFF_CHIC_CMU1.5_PT1.5_TRK" trigger can be broken down to the Level 1, 2 and 3 trigger efficiencies. Level 3 is a software trigger with the efficiency estimated to be 100% [32]. Level 2 is auto-accept which by definition has 100% efficiency. The Level 1 trigger is comprised of a CMU low pT muon trigger (CMU1.5_PT1.5) plus a BSC gap trigger (TWO GAP). The BSC gap trigger was measured to be ~ 100% [32]. To measure the efficiency of CMU1.5_PT1.5, we used the method coded in the CDF MuonUser package, which is developed and maintained by the B physics group [35] [36]. Note that the curve shown in Figure 32 is for one single muon. For a dimuon event, the probability of firing the L1_CMU1.5_PT1.5 trigger is calculated using:

$$P_{\mu\mu} = 1 - (1 - \mathrm{p1}) \times (1 - \mathrm{p2}) \tag{1}$$

where p1, p2 are read off the curve according to the pt of the two muons. Table 7 summarizes the trigger efficiency for dimuon events based on (1).

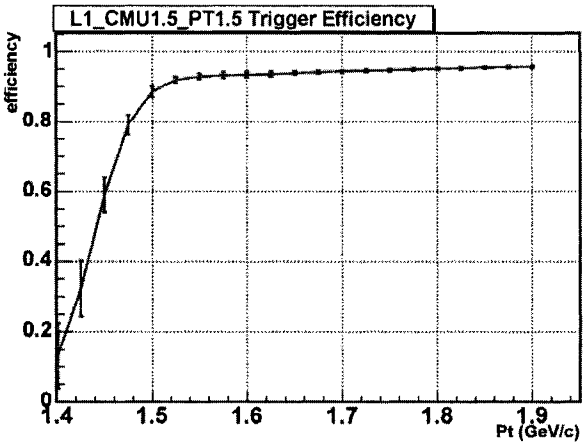

Figure 32: L1 CMU1.5_PT1.5 Trigger Efficiency as function of each muon pT

	ε_{L1}
$\gamma\gamma \to \mu\mu$	**99.5 ± 0.5 %**
$J/\Psi \to \mu\mu$	**98.2 ± 1.1 %**
$\Psi' \to \mu\mu$	**99.6 ± 0.4 %**

Table 7. summary of "event-based" L1_CMU1.5_PT1.5 trigger efficiency

4.2.3 Muon quality cuts Efficiency

To measure this efficiency, we utilized clean $J/\Psi \rightarrow \mu\mu$ events from the gdifah and gdifai data, as well as the Monte Carlo events after detector simulation. The method employed was to put strong muon quality cuts on one muon and test whether or not the other muon would pass our quality cuts. In order to define the clean J/Ψ muon-pair events the following cuts were employed:

(1) Muon pseudorapidity, $|\eta| < 0.6$;
(2) Cosmic ray cut, $\Delta(\mathrm{ToF}) < 3\mathrm{ns}$;
(3) Vertex cut, $\Delta(Z_0) < 5$ cm;
(4) Opposite charges of the two muons, $Q_{\mu 1} * Q_{\mu 2} = -1$;
(5) Isolation energy in a cone of R=0.4 around the muons tower, excluding the muon tower, is less than 0.1 GeV.

Figure 33 shows the result of the selection described above, and we then use the events in the clean J/Ψ peak to examine our muon quality cuts. As a second method we use the STARLIGHT and LPAIR Monte Carlo events, after detector simulation and reconstruction, to examine the muon quality cuts. Figure 34 shows the efficiency of the offline muon quality cuts as function of dimuon mass (top), dimuon P_T, dimuon rapidity, for muonpairs from J/Ψ, ψ' and the QED continuum. In Figure 35 we see the variation of the efficiency of the offline muon quality cuts as function of muon η (left), muon ϕ (right) and muon pT (top) for muons from J/Ψ, ψ' and the QED continuum. Table 8 summarizes the overall muon quality cuts efficiency.

	ε_Q
$\gamma\gamma \rightarrow \mu\mu$	**41.82 ± 2.30 %**
$J/\Psi \rightarrow \mu\mu$	**33.36 ± 1.70 %**
$\Psi' \rightarrow \mu\mu$	**44.82 ± 5.64 %**

Table 8. summary of the overall muon quality cuts efficiency

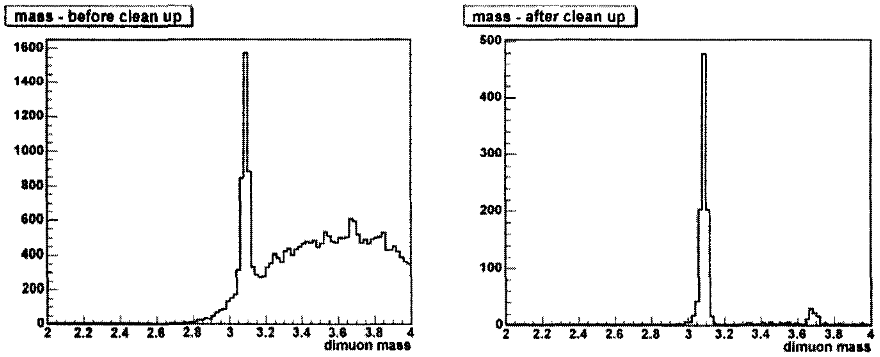

Figure 33: The muon-pair mass distribution before and after strong muon quality cuts

4.2.4 Cosmic veto cuts Efficiency

A very small portion of the signal events may have opening angles close to π and do not have both valid TOF information, thus they may be killed by the cosmic veto cuts. The fraction of such events is examined with STARLIGHT Monte Carlo event, and is found to be to < 0.1% for $\gamma\gamma \rightarrow \mu\mu$, < 0.2% for $J/\Psi \rightarrow \mu\mu$ and < 0.2% for $\Psi' \rightarrow \mu\mu$.

4.2.5 Exclusive Efficiency and Effective Luminosity

Exclusivity cuts are used to determine whether an event is exclusive or not. As a set of offline cuts, it should have 100% efficiency. In other words, suppose we have perfect detector, perfect trigger system, perfect offline reconstruction and all other offline cuts are perfect, all available exclusive dimuon events will be found, i.e. all of them will pass the exclusivity cuts. Any loss of true exclusive events does not come from the exclusivity cuts itself.

There are actually a significant part of exclusive events that do fail the exclusivity cuts, that's because: (1) high luminosity introduces multi-interactions in one beam crossing, i.e. another event happened in the same bunch crossing of an exclusive dimuon event, and made it fail the exclusivity cuts; (2) there is noise in the detector that results in the event failing the exclusivity cuts. Thus, we need to know, during period 1-11, in how many beam crossings (or one can say how much time) can the detector detect an exclusive dimuon event if it is present.

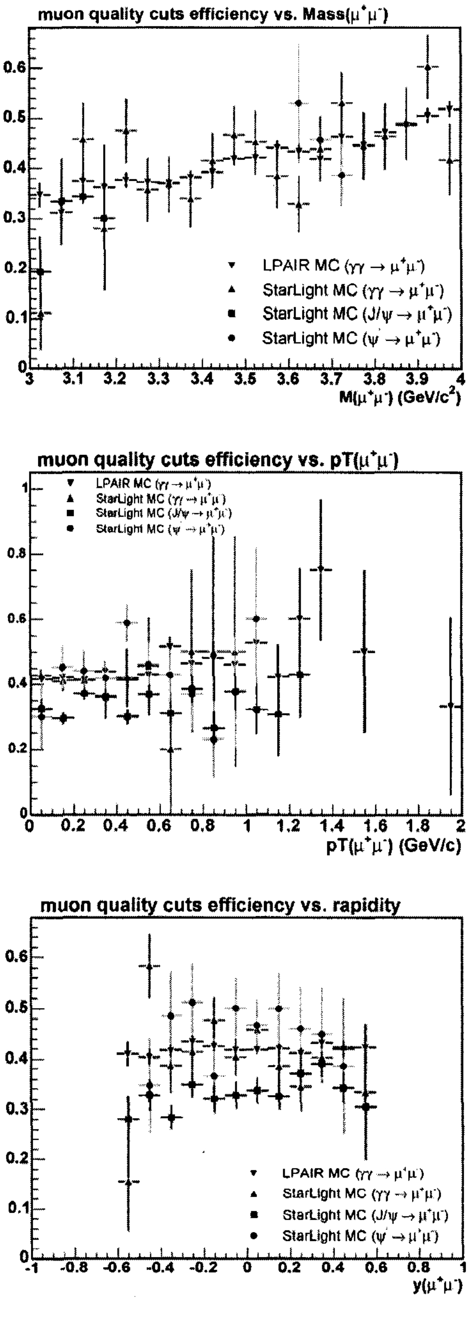

Figure 34: Offline muon Quality cuts Efficiency as function of dimuon mass (top), dimuon P_T (middle), dimuon rapidity (bottom), for muon-pairs from J/ψ, ψ' and the QED continuum.

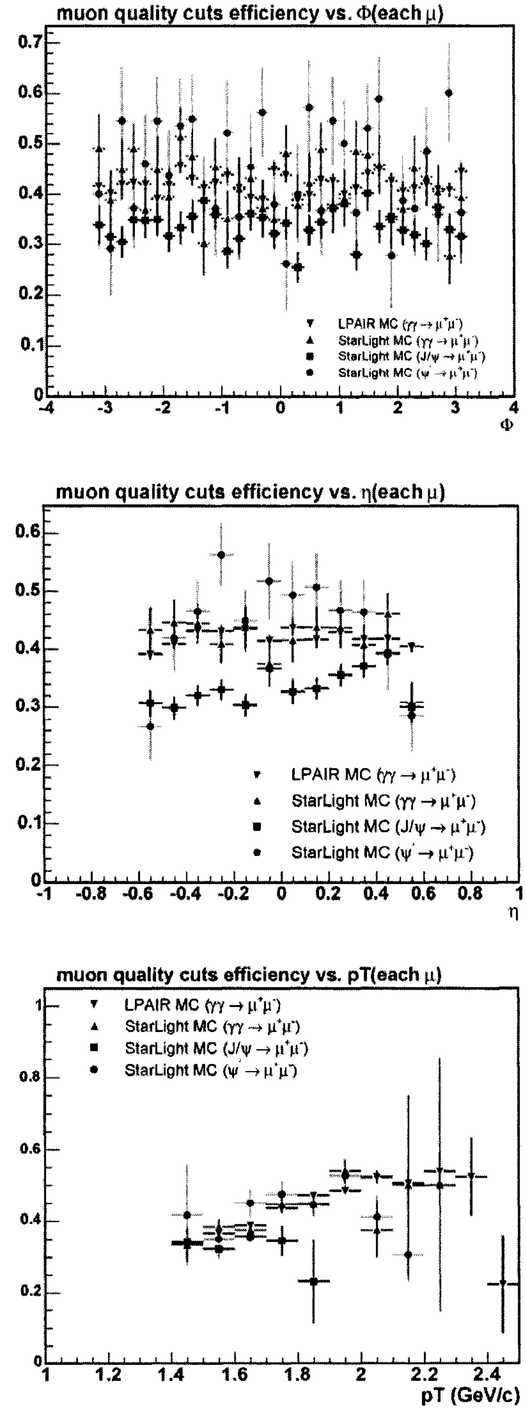

Figure 35: Offline Muon Quality cuts Efficiency as function of muon ϕ (middle), muon η (bottom) and muon P_T (top) for muons from J/ψ, ψ' and the QED continuum.

So the so-called "exclusive efficiency" is essentially the fraction of time that the detector can detect exclusive events. We use zero-bias events to measure this efficiency. For example, suppose we have 100 zero bias events (i.e, 100 beam crossings), if there is a hit in any CDF detector in 30 out of the 100 crossings, that means the exclusive signal cannot be measured for 30% of the time, because those events have hits in the detector that cause them to fail the exclusivity cuts. The hits in those 30 events could be due to detector noise and/or beam background and/or multi-collisions. Thus, the exclusive signal can be observed only 70% of the time during that period. Therefore, to get the correct cross section, the number of observed exclusive dimuon events has to be multiplied by 1/0.7. It is equivalent to correct the luminosity by multiplying 0.7, which is called "Effective Factor". In our cross section calculation we choose to multiply this 0.7 by the integrated luminosity and define it as "Effective Luminosity", where Effective Luminosity equals the product of the "Effective Factor" with the "Integrated Luminosity".

To get the effective factor from zero-bias data, we check the fraction of events that passed the exclusivity cuts. This fraction decreases exponentially as function of bunch luminosity as shown in Figure 36 (up). Then multiply the fraction by the bunch luminosity distribution to get a new distribution, shown as the shaded area in Figure 36 (down). Then the effective factor is the shaded area divided by the open area of bunch luminosity distribution. It is important to do this over the same run range as the data, since the beam effects and electronic noise are run dependent. Figure 36 shows the variation of ε_{exc} with bunch luminosity for period 8 (up). Also shown (down) is bunch luminosity for zero-bias data, the bunch luminosity weighted with exclusivity efficiency and the variation of exclusivity efficiency with bunch luminosity. Table 9 shows the luminosity and effective luminosity, for the analysis described in this thesis, as a function of run period.

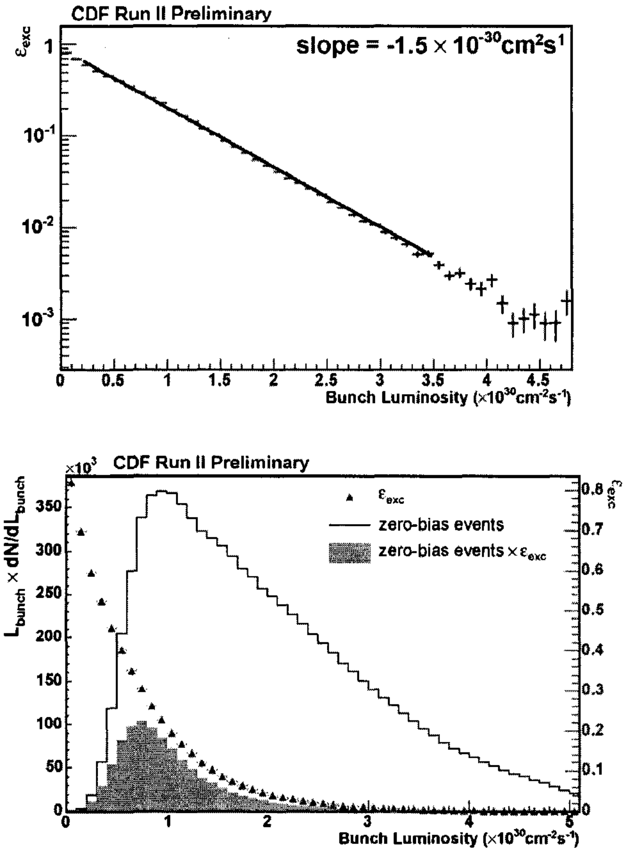

Figure 36: The variation of exclusive efficiency with bunch luminosity for period 8 (left). Also shown (right) is bunch luminosity for zerobias data, the bunch luminosity weighted with exclusive efficiency and the variation of exclusive efficiency with bunch luminosity.

Period	Intercept	Slope	Effective factor: f	Integrated luminosity: L (pb^{-1})	$f \times L$	$N_{observed}$	$\frac{N_{observed}}{f \times L}$
1	0.68	-2.25	0.0788	114.2	9.0	32	3.56
2	0.81	-2.05	0.0886	116.3	10.3	31	3.01
3	0.86	-1.90	0.1166	86.5	10.1	28	2.77
4	0.87	-1.70	0.1157	66.1	7.7	24	3.12
5	0.89	-1.66	0.1231	127.9	15.7	46	2.93
6	0.91	-1.57	0.1144	97.9	11.2	32	2.86
7	0.94	-1.50	0.1598	29.5	4.7	11	2.33
8	0.92	-1.50	0.1152	179.4	20.7	61	2.95
9	1.01	-1.47	0.0881	166.5	14.7	41	2.79
10	1.04	-1.44	0.0765	258.5	19.8	55	2.78
11	0.98	-1.37	0.0611	241.7	14.8	41	2.77
SUM				1484.4	138.6	402	

Table 9: Table of luminosity and effective luminosity as a function of run period

4.2.6 Fit to the Invariant Mass Distribution

After the muon quality cuts, cosmic veto cuts and exclusivity cuts 402 exclusive dimuon events from period 1-11 data remained, as shown in Figure 37. These events predominantly arise from the following sources, two-photon production of continuum $\mu+\mu-$ pairs and the photoproduction of the vector mesons J/ψ and ψ′ subsequently decay into muon pairs. The invariant mass distribution between 3.0 GeV/c^2 and 4.0 GeV/c^2 was fitted to two Gaussians representing the vector mesons states plus an exponential function representing the QED continuum. The fit function has the following form:

$$Y = (p0 \cdot e^{\frac{-(x-p1)^2}{2\cdot(p2)^2}}) + (p3 \cdot e^{\frac{-(x-p4)^2}{2\cdot(p5)^2}}) + A \cdot F_{QED} \cdot F_{AE}$$

where,

$$F_{QED} = e^{-0.852\cdot x};\ F_{AE} = 0.6 - 0.5 \cdot e^{-3.22\cdot(x-3.05)}$$

In these equations, P_1 is the centre of the J/ψ invariant mass peak, P_0 and P_2 are the height and width of the J/ψ peak, respectively. In the case of the ψ′, P_4 is the centre of the ψ′ invariant mass peak, and P_3 and P_5 are the height and width of the ψ′ peak, respectively. The variable: A gives the area under the QED continuum distribution, and thus the number of events in the continuum. The height and width of the two Gaussian peaks give the number of J/ψ and ψ′ events. From this fit the number of events, for the standard analysis and exclusivity cuts, is 286.5 ± 17.1 J/ψ events, 38.5 ± 6.8 ψ′ events, and 77.3 ± 9.6 events in the QED continuum.

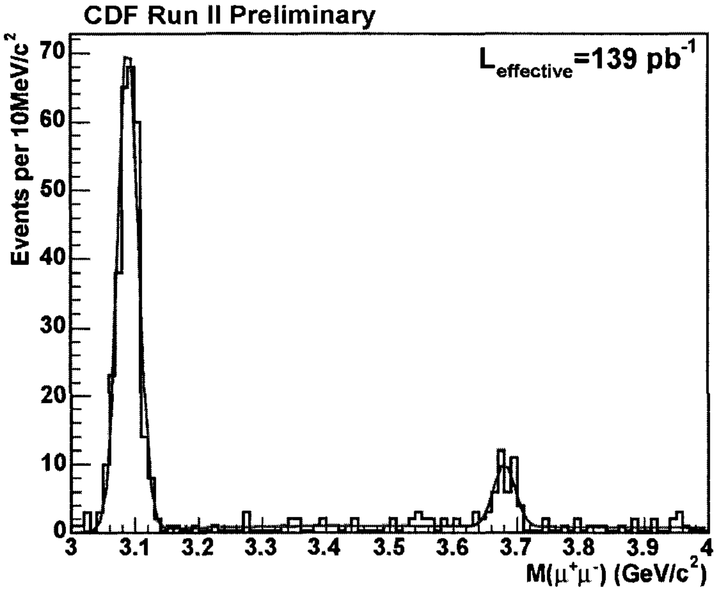

Figure 37: The fit to the invariant mass distribution.

Finally, Table 10 summarizes the efficiencies calculated in this section.

	$\varepsilon_{det.rec}$	ε_{L1}	ε_Q	ε_{cosmic}	ε_{all}
$\gamma\gamma \rightarrow \mu\mu$	41.8 ± 1.5%	99.5 ± 0.5%	41.8 ± 2.3%	99.9 ± 0.1%	17.4 %
$J/\Psi \rightarrow \mu\mu$	18.8 ± 0.3%	98.2 ± 1.1%	33.4 ± 1.7%	99.8 ± 0.2%	6.2 %
$\Psi' \rightarrow \mu\mu$	53.9 ± 2.8%	99.6 ± 0.4%	44.8 ± 5.6%	99.8 ± 0.2%	24.0 %

Table 10. Summany of major efficiencies ($\varepsilon_{all} \equiv \varepsilon_{det.rec} \cdot \varepsilon_{L1} \cdot \varepsilon_Q \cdot \varepsilon_{cosmic}$)

4.3 Background Processes

There are four backgrounds to consider:

(1) **χ_c background** due to the decays of the $\chi_c^0 \rightarrow J/\psi(\rightarrow \mu^+\mu^-) + \gamma(\text{soft})$, where the soft photon is either missed or has an energy underneath the exclusivity cuts.

(2) **Exclusivity background** due to inclusive processes (i.e. Drell-Yan) that are observed as exclusive due to particles not being observed in the calorimeters (i.e. falling into cracks in the detector or being too soft to reach any detectors).

(3) **Cosmic background** due to cosmic rays occuring in time with the beam crossing

(4) **Dissociation background** due to inelastic events where the dissociation products are too far forward to be detected by the BSCs.

4.3.1 χ_c background for J/ψ photoproduction

A J/ψ in the final state can also arise from exclusive χ_c production, where $\chi_c^0 \rightarrow J/\psi(\rightarrow \mu^+\mu^-) + \gamma(\text{soft})$. In this Double Pomeron Exchange process $p + \bar{p} \rightarrow p + \chi_c + \bar{p}$ the photon in the χ_c decay, having a maximum energy ~500 MeV/c^2, is often too soft to be reconstructed. In this case the χ_c channel is a source of background to exclusive J/ψ production via photon-pomeron fusion. A search for the process $p + \bar{p} \rightarrow p + \chi_c + \bar{p}$ itself was performed in CDF previously, but the result was not published. Using 93 pb^{-1} (delivered luminosity) taken by a dimuon trigger, 13 exclusive J/ψ events and 10 $J/\psi + \gamma$ events were observed that contain nothing else visible in the full detector including the very forward regions. These 10 $J/\psi + \gamma$ events were reported as being consistent with originating from χ_c decays.

The main difficulty for searching $p + \bar{p} \rightarrow p + \chi_c + \bar{p}$ is that the CDF detector simulation is unreliable for very low energy photons, thus it's hard to estimate the detector efficiency and reconstruction efficiency. We have generated the $\chi_c^0 \rightarrow J/\psi(\rightarrow \mu^+\mu^-) + \gamma$ events using the ChiC Monte Carlo program, and put the MC events through detector simulation. We found ~30% of the soft photons were killed by detector simulation program, i.e. there are no EM Towers with non-zero energy deposited in a cone of 0.3 around the gen-level (gen-level means before detector simulation) photon direction. Figure 38 (left) shows the gen-level photon energy distribution of those ~30% events that have zero EM energy in the direction of gen-level photon. The other ~70% of the events, after detector simulation, has some EM energy in the direction of gen-photon. Figure 38 (right) shows the reconstructed max Em tower energy (in cone of 0.3 around gen-photon) vs. the gen-photon energy.

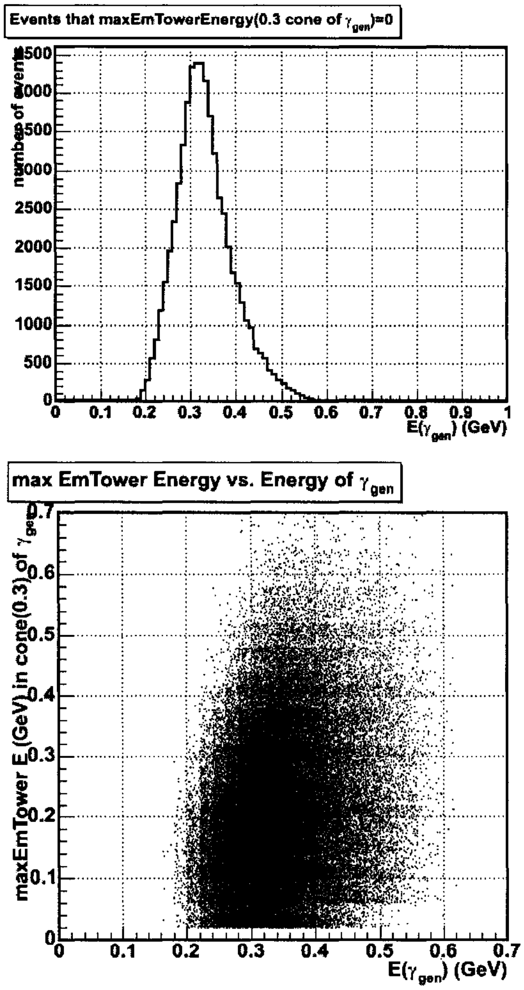

Figure 38. Gen-level photon energy distribution (left) of those events that have zero Em energy in the direction of gen-photon. Reconstructed maximum EM tower energy (in cone of 0.3 around gen-photon) vs. the gen-photon energy (right).

In the present analysis we use two new methods, which are independent of photon reconstruction and independent of each other, to cope with this difficulty. The first approach is based on the expected difference in shapes of the P_T and $\Delta\phi$ distribution of the dimuons from J/Ψ photoproduction and χ_c decay. The second method is based on an extrapolation of the change in the number of events with decreasing EM exclusivity cut (in the central and end-wall region).

Method 1 (histogram method):

The first method is based on the expected difference in shapes of the P_T and $\Delta\phi$ distribution of the dimuons from J/ψ and χ_c decay. The J/ψ from χ_c decay has a larger mean P_T, and a larger deviation from $\Delta\phi = \pi$. These two are strongly correlated for two reasons: photon emission from $p(\bar{p})$ has generally much lower P_T than pomeron emission, and when the χ_c decays it gives a further "kick" to the J/ψ. We assume that the observed dimuon events come from only two sources: J/ψ photon production ($\gamma\mathbb{P}$) and J/ψ from χ_c decay ($\mathbb{P}\mathbb{P}$), and simulate the two processes with Monte Carlo events generator and CDF detector simulation. The P_T (or $\Delta\phi$) distributions from the two Monte Carlos are then summed with weight f and (1-f), where f $\in(0,1)$, and a statistical χ^2-test is performed between the real data and the sum of two Monte Carlos. The value of "f" that corresponding to the minimum χ^2 gives the most likely combination of the two processes.

In practice the kinematics of χ_c production and decay were simulated by the ChiC Monte Carlo and that of the photoproduced J/ψ by the STARLIGHT Monte Carlo. Both sets of events were then passed through the mcProduction 6.1.4 (i.e. detector simulation plus offline reconstruction). The procedure was performed for (a) the standard analysis cuts with ***all*** exclusivity cuts (where EM exclusivity cut in central and plug regions = 80MeV); (b) the standard analysis cuts with all exclusivity cuts ***except*** the EM exclusivity cuts in the central and end-wall region, thus allowing all photons from χ_c decay. For either (a) or (b), we sum the P_T (or $\Delta\phi$) distributions (i.e. histograms) from ChiC MC and STARLIGHT MC according to this formula (bin by bin):

$$N_i = A(f) \cdot [f \cdot N_i^{J/\psi} + (1-f) \cdot N_i^{\chi c}], \quad f \in [0,1]$$

where, $N_i^{J/\psi}$ is the number of events in the ith bin of the STARLIGHT MC distribution, and $N_i^{\chi c}$ is the number of events in the ith bin of the ChiC MC distribution. For each given f, A(f) is determined to equalize the area of the observed data distribution and the area of the sum of the two MC distributions, then N_i is determined for each bin of the "MC-sum" distribution. Finally we performed the χ^2-test between the data distribution and MC-sum distribution, to see what combination (f) gives best χ^2. The χ^2 between two histograms is defined as:

$$\chi^2(f) = \sum_i \frac{(\,\mathrm{data}(i) - \mathrm{MCsum}(i)\,)^2}{\mathrm{data}(i) + \mathrm{MCsum}(i)}$$

where the sum of "i" is from the first bin to the last bin of the histogram. The variations of the χ^2-test result as function of "f" are shown in Figure 39 and Figure 40 for $\Delta\phi$ and P_T distributions, respectively, where all exclusivity cuts were applied. A clear minimum of χ^2 was observed in both distributions, corresponding to (f =) 64% ± 20% for $\Delta\phi$ and 67% ± 20% for P_T. These numbers represent the estimated fraction of dimuons from J/ψ photoproduction, under the 80MeV EmEt exclusivity cuts in central plus plug regions. In the above results, the 1σ uncertainty on f is given by the two f-values at $\chi^2(\min) + 1$.

We now repeat the kinematics histogram fitting for J/ψ events with an EM tower (or pair of adjacent EM towers) with EmEt>80 MeV, i.e. the events that was killed by the 80MeV EmEt exclusivity cuts in central plus plug regions. This sample of events should have no photoproduced J/ψ, only χ_c. The $\Delta\phi$ and P_T histograms (with the best fit f-value) and $\chi^2(f)$ distributions are shown in Figure 41 and Figure 42. Both the $\Delta\phi$ distribution and the P_T distribution find f = 0 as the best fit (as the minimum is at f<0, the upper limit is not well defined).

While this method is not very sensitive, and is dependent on the STARLIGHT and CHIC Monte Carlo predictions of the kinematics, it does show that the χ_c background in the exclusive sample is consistent with being small, and that the J/ψ background above the 80MeV EmEt exclusivity cut is probably negligible. We carry forward from this method a fraction (0.34 ± 0.22) of the observed signal events in the J/ψ peak under exclusive cuts to be χ_c background. The results of this method is summarized in Table 11.

	N = observed events in J/ ψ mass window	f = the fraction of photoproduced J/ψ	N × f (photoproduced J/ψ)	N × (1-f) (J/ψ from χ_c decay)
EmEtCut=80MeV	286.5 ± 17.1	0.66 ± 0.2	197.7 ± 64.1	88.7 ± 63.3

Table 11. Results of Method

Method 2 (extrapolation method):

If the EM exclusivity cuts in the central and end-wall region are increased from EmEt= 80 MeV up to 600 MeV, more and more $\chi_c \rightarrow J/\psi + \gamma$ events (if present) will be accepted. This is indeed the case for the J/ψ peak, as shown in Table 12. Removing the EmEt cut altogether (600 MeV → ∞) finds no more events. The fit number of ψ' events increases only from 38.5 to 40.0, i.e. only 4% of the ψ' have an EM tower above 80 MeV, they are very clean. The fit number of QED events increases from 77.3 at 80 MeV to 81.9 at 150 MeV and to 84.7 at 500 MeV, with no more above that. We do not know why there would be more associated photons with the QED sample than the ψ' sample, but a similar observation was made from the tails in the P_T and $\Delta\phi$ distributions (for the events *under* the 80 MeV cut). We attribute both these types of events to non-exclusive background.

The method is based on an extrapolation of the change in the number of events ΔN with decreasing EM exclusivity cuts in Central and EndWall region. A graph of this variation is shown in Figure 43. The form of the variation of ΔN with EmEt cut was fitted to the form:

$$\mathbf{N = P_0 - P_1 \cdot e^{-P_2 \cdot EmEtCut}}$$

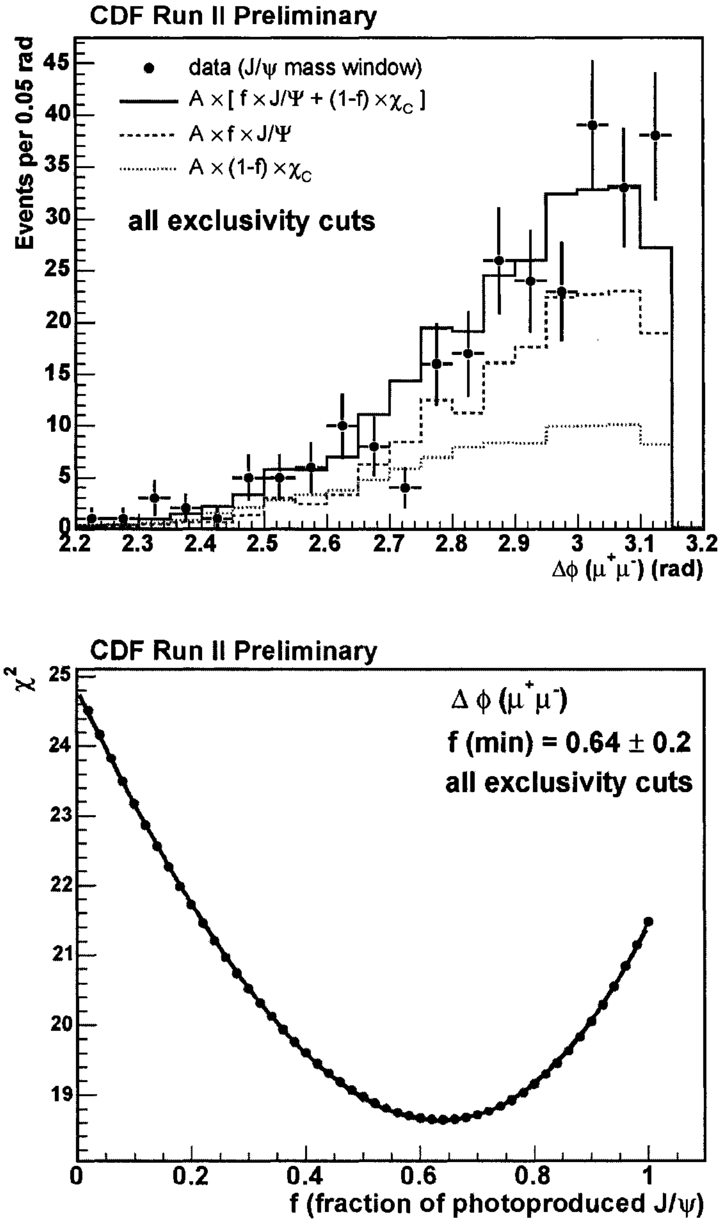

Figure 39: The χ^2 Test values (bottom) for different combinations of **Δφ** from STARLIGHT MC (photoproduced J/ψ) events and CHIC MC events. The blue histogram (top, solid) is the sum of STARLIGHT MC (top, dashed) and CHIC MC (top, dashed) with a fraction **f = 0.64**, which corresponds to the minimum χ^2 value. **All exclusivity cuts** were applied to real data and MC data.

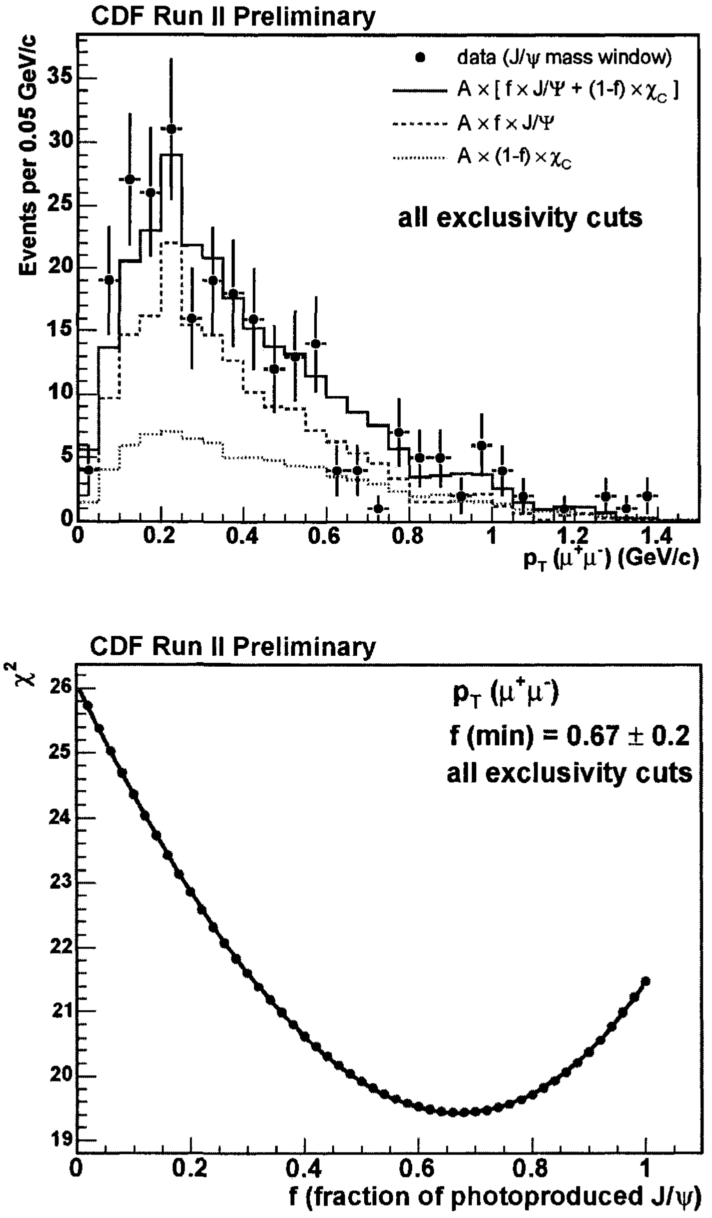

Figure 40: The χ^2 Test values (bottom) for different combinations of $\mathbf{P_T}$ from STARLIGHT MC (photoproduced J/ψ) events and CHIC MC events. The blue histogram (top, solid) is the sum of STARLIGHT MC (top, dashed) and CHIC MC (top, dashed) with a fraction **f** = **0.67**, which corresponds to the minimum χ^2 value. **All exclusivity cuts** were applied to real data and MC data.

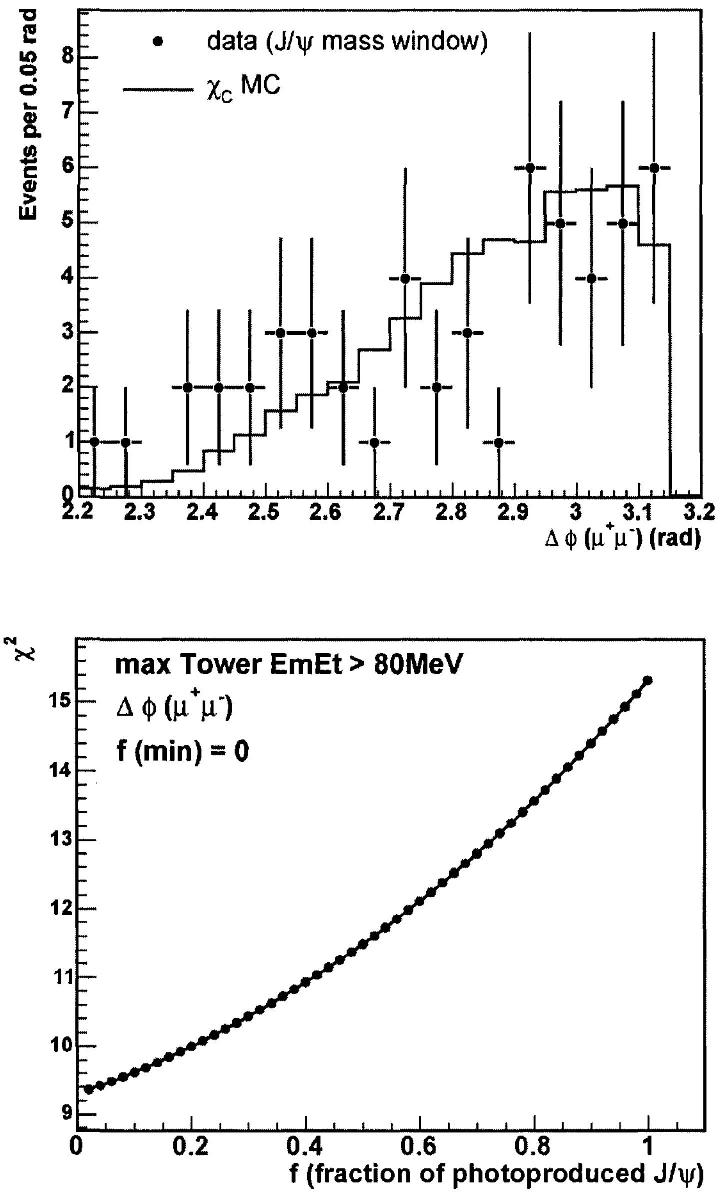

Figure 41: The χ^2 Test values (bottom) for different combinations of **Δφ** from STARLIGHT MC (photoproduced J/ψ) events and CHIC MC events. The χ^2(f) curve shows that the best fit is at f<0, which means all these dimuon events are χ_c-like. The blue histogram (top, solid) is the CHIC MC.

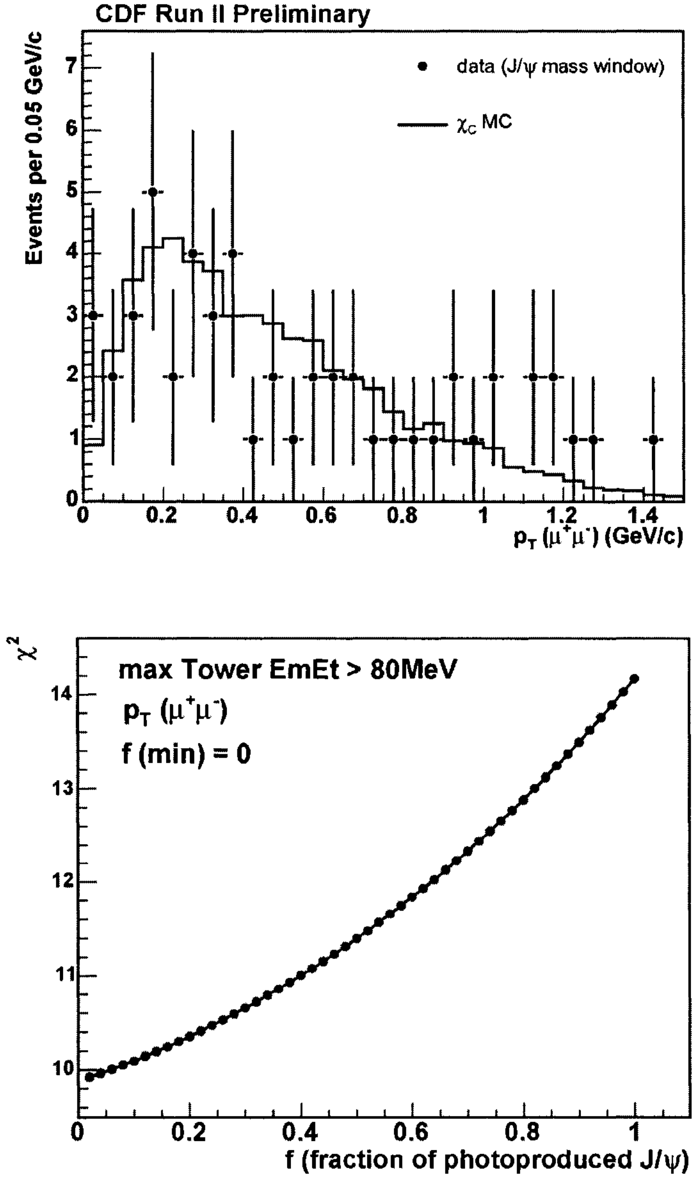

Figure 42: The χ^2 Test values (bottom) for different combinations of **P_T** from STARLIGHT MC (photoproduced J/ψ) events and CHIC MC events. The χ^2(f) curve shows that the best fit is at f<0, which means all these dimuon events are χ_c-like. The blue histogram (top, solid) is the CHIC MC.

- When EmEtCut = ∞, N = P_0, this is the total number of observed dimuon events in J/ψ mass window, which includes all photoproduced J/ψ and all J/ψ from χ_c decay.
- When EmEtCut = 0, N = P_0 - P_1, this is the total number of photoproduced J/ψ (P_1 is the total number of χ_c events).
- When 0 < EmEtCut < ∞, $(\mathbf{P_0} - \mathbf{P_1} \cdot \mathbf{e}^{-\mathbf{P_2}\cdot\mathbf{EmEtCut}}) - (\mathbf{P_0} - \mathbf{P_1}) = \mathbf{P_1} \cdot (\mathbf{1} - \mathbf{e}^{-\mathbf{P_2}\cdot\mathbf{EmEtCut}})$ gives the number of χ_c under EmEtCut.

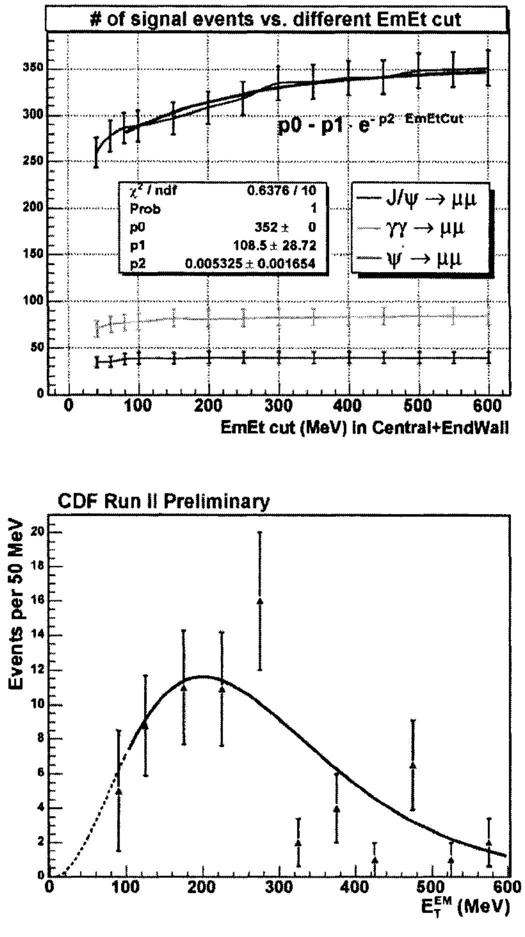

Figure 43: The variation of observed number of events in the J/ψ mass window (top), ψ' mass window (bottom) and QED continuum mass window (middle), with different EM exclusivity cut values in the central and end-wall region. The lower plot is the differential of the upper plot.

EmEt cut in Central+EndWall	N(J/ψ)	N(ψ′)	N($\gamma\gamma$)
40 MeV	260.4 ± 16.0	34.9 ± 6.5	71.0 ± 9.1
60 MeV	278.2 ± 16.8	35.6 ± 6.6	75.5 ± 9.4
80 MeV	286.5 ± 17.1	38.5 ± 6.8	77.3 ± 9.6
100 MeV	288.5 ± 16.8	39.5 ± 6.8	78.4 ± 9.4
150 MeV	297.3 ± 17.4	39.1 ± 6.9	81.9 ± 9.8
200 MeV	308.3 ± 17.7	40.2 ± 6.9	81.8 ± 9.8
250 MeV	319.2 ± 17.8	40.2 ± 6.9	81.9 ± 9.7
300 MeV	335.2 ± 18.5	40.1 ± 6.9	83.0 ± 9.9
350 MeV	337.2 ± 18.5	40.1 ± 6.9	83.0 ± 9.9
400 MeV	341.2 ± 18.2	40.0 ± 6.9	84.1 ± 9.7
450 MeV	342.2 ± 18.6	40.0 ± 6.9	84.1 ± 10.0
500 MeV	348.7 ± 18.8	40.0 ± 6.9	84.7 ± 10.0
550 MeV	349.7 ± 18.9	40.0 ± 6.9	84.7 ± 10.0
600 MeV	351.7 ± 18.9	40.0 ± 6.9	84.7 ± 10.0
no cut	351.7 ± 18.9	40.0 ± 6.9	84.7 ± 10.0

Table 12. Number of observed exclusive dimuon events (from fit)
for different EmEt exclusivity cut in Central+Plug regions

The fit should be made only for data at EmEtcut$\geq$80 MeV and for P0 fixed at 352 (the number of observed events in J/ψ mass window with no EM cut), as shown in Figure 43 upper plot. The results are summarized in Table 13. However, the Figure 43 upper plot has strong correlation between adjacent points as each point contains the events in previous point. So we made the differential plot of Figure 43 upper plot, and the result is the Figure 43 lower plot. The statistic of the differential plot is low, but we can fit this with a reasonable (empirical) parameterization, which is the product of a rising power with a falling exponential. We actually fit it to the following form:

$\mathrm{N(events/50MeV)} = \mathrm{A} \times \mathrm{EmEt}^{\mathrm{B}} \times \mathrm{e}^{-\mathrm{C}\times\mathrm{EmEt}}$, where A, B, C are free

The best fit gives: A = 0.00025, B = 2.5, C = 0.0125. The integral of the fit curve gives 68.2 events, where 2.8 events are below 80 MeV and 65.4 events are above 80 MeV. We actually observed 65.2 events above 80 MeV (65.2 = 351.7 - 286.5 from Table 12), and the histogram method (Figure 41-42) indicates they are all χ_c-like. So, for the extrapolation method, we get the conclusion that only 2.8 events under the 80 MeV exclusivity cut are from χ_c decay.

	Fit range (EM cut)	**P_0**	**P_1**	**P_2**	**$P_1 \cdot (1 - e^{-P_2 \cdot 80MeV})$**
P_0 fixed	80 MeV	352±0	109±29	$(5.3\pm1.7)\cdot10^{-3}$	38±14

Table 13

The histogram method of P_T and $\Delta\phi$ gave consistent result, which suggests that ~1/3 of the signal events under the observed J/ψ mass peak are coming from χ_c decay, but we trust it less than the extrapolation method. That's because the extrapolation method, especially the differential EmEt plot, is purely based on experimental data, it's not dependent on Monte Carlo model and it has much smaller uncertainty. The differential EmEt plot yields only 2.8 χ_c-like dimuon events under the 80 MeV EmEt exclusivity cut, and we carry this result to the final cross section calculation.

4.3.2 Exclusive background

The χ_c^0 background discussed above is essentially an exclusivity background. In this case one exclusive process i.e. $\chi_c^0 \rightarrow J/\psi + \gamma$ mimics exclusive photoproduction of J/ψ because the soft photon is missed. The exclusivity background considered here is generated by inclusive processes, such as Drell-Yan production, that appear to be exclusive because some particle(s) pass through cracks in the calorimetry coverage or leave energy depositions that fall below the noise threshold cuts.

Qualitatively speaking the exclusivity background is not expected to be large since the agreement between the predicted and observed number of $\gamma\gamma \rightarrow \mu^+\mu^-$ events is good. In this case the predictions for this exclusive final state (a well understood QED process) by STARLIGHT and LPAIR are in agreement and are theoretically expected to be reliable. Also, the excellent description of the shape of the kinematic distributions, particularly the P_T and $\Delta\phi$ distributions - for the ψ' and the QED continuum, show no evidence for a significant exclusivity background. Since one would expect to see evidence for events with unexpectedly large P_T and/or a $\Delta\phi$ that is not consistent with the observed muon pair being back to back.

In Table 10 the number of J/ψ, ψ' and QED continuum events, after a set of increasing central and end-wall EM eclusivity cuts, is tabulated. The numbers of events were obtained from a fit to the invariant mass spectrum of exclusive muon-pair candidates as described in section 4.2.5. Considering first the J/ψ signal we see the rise in the number of events with exclusivity cut due to the presence of a background from the χ_c^0, as explained above. However, the number of events in the ψ' peak and the QED continuum remains flat when the EM exclusivity cut in the central and end wall region is set at ~100 MeV and above. This would be expected with at most a small exclusivity background in the ψ' and the QED continuum candidate events. If there were a sizeable number of exclusivity background events contaminating these samples we would expect a rising distribution, as seen in the J/ψ case, as more and more background events survived the increasing (in value) EM exclusivity cut.

The correlation between $\Delta\phi$ and P_T for the various channels contributing to the muon-pair data is shown in Figure 44. Using the above mentioned arguments the exclusivity background is expected to lie in the tails of the P_T and $\Delta\phi$ distributions. As these distributions are highly correlated we can combine them into a single "V" variable, as illustrated in Figure 45, where the U and V axes are defined by the equations:

$$u = \sin(\theta) \cdot \Delta\phi + \cos(\theta) \cdot p_T$$

$$u = -\cos(\theta) \cdot \Delta\phi + \sin(\theta) \cdot p_T$$

where, $\theta = \tan^{-1} [2/M(\mu^+\mu^-)]$. The resulting distribution of V variable is shown in Figure 46 and the percentage of MC generated signal events that eliminated by an increasing cut in the V variable (V_0) is also shown in Figure 46.

Using MC samples of the three channels we can define an exclusivity cut based on a V-cut that rejects 2% or 4% of the events, respectively. Data events above the V-cut, in the tails of the P_T and/or the $\Delta\phi$ distributions, are considered to be non-exclusive background.

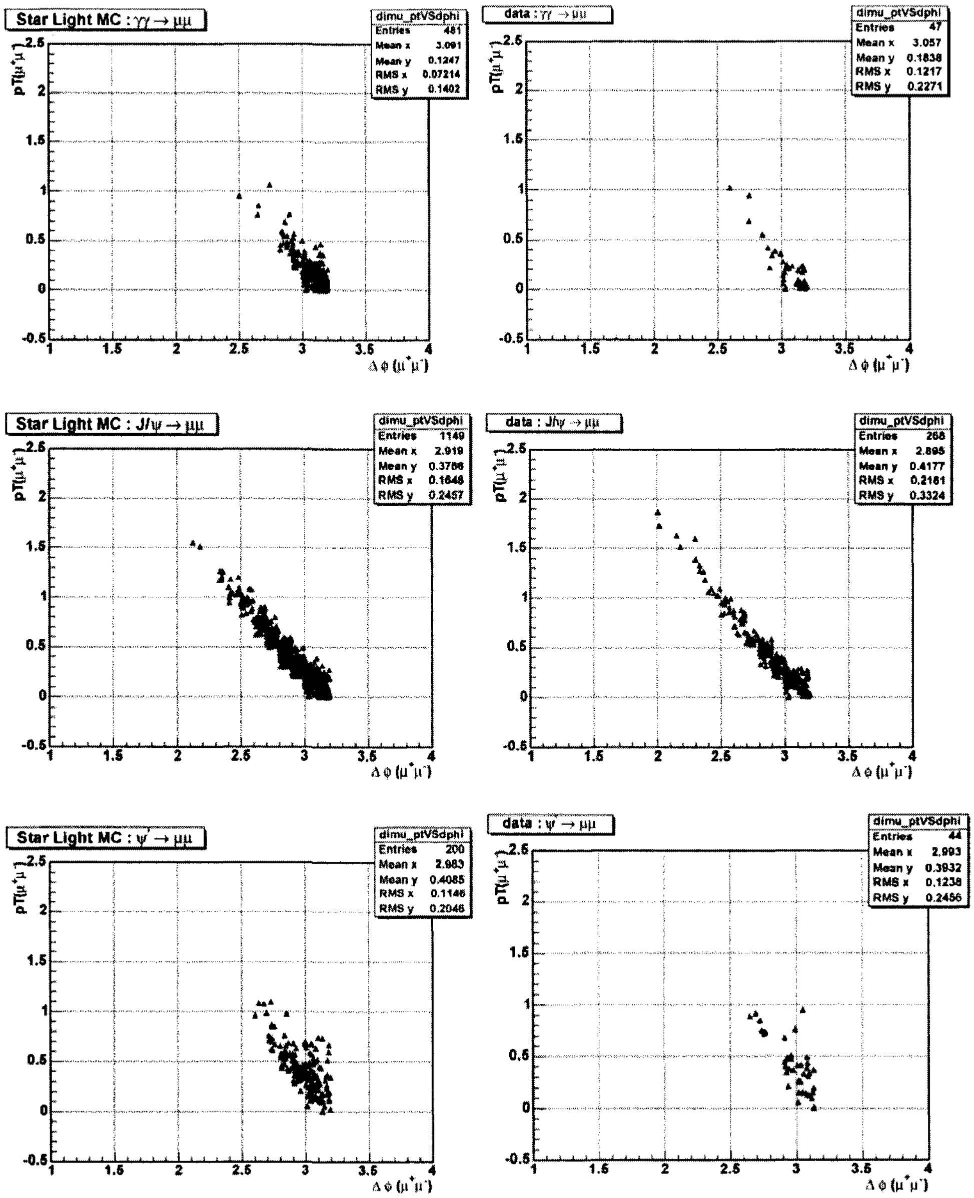

Figure 44: The correlation between $\Delta\phi$ and P_T for the various channels contributing to the muon-pair data.

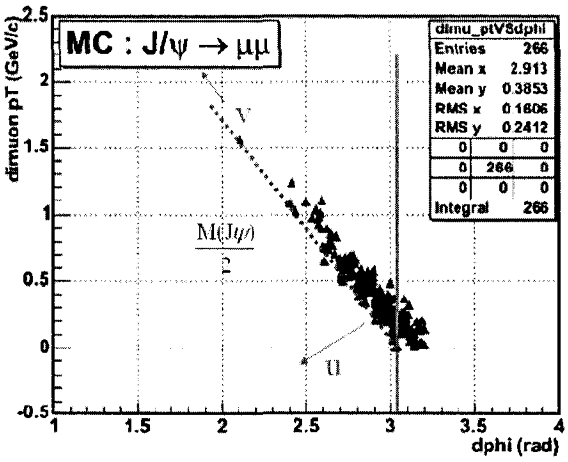

Figure 45: The scatter plot illustrating the definition of the "V" variable.

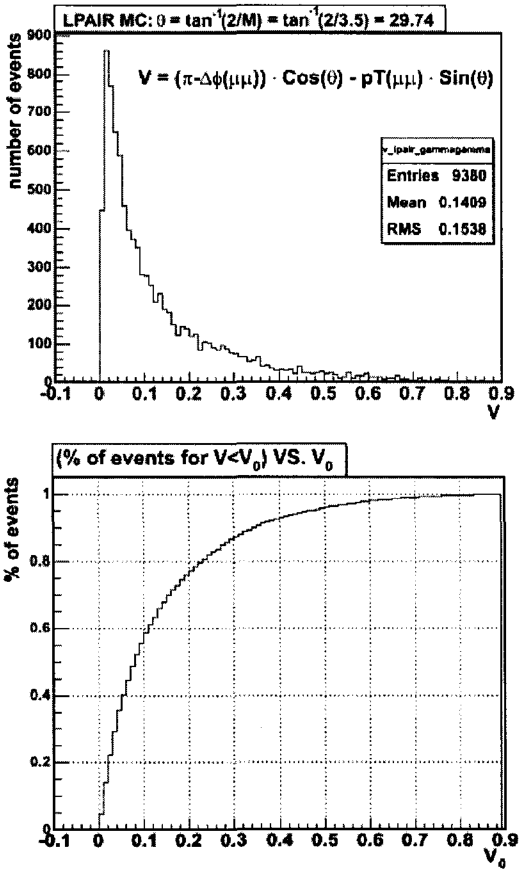

Figure 46: The distribution of the V-variable (left); and the percentage of events cut as a function of the cut (V_0) (right)

4.3.3 Dissociation background

The dissociation background accounts for events that appear to be truly exclusive, but one or both of the protons is excited into a low mass state and then dissociates. It is possible for these dissociated events to be very forward, and unobserved in the CDF detector. The inelastic running mode of the LPAIR MC is used to estimate this background. Unfortunately, the LPAIR MC only provides the kinematics of the dissociating proton, it does not actually dissociate the proton into partons. In order to do this, a function called 'fragment cluster' from Minimum Bias Rockefeller (MBR) MC [37] is used. This function fragments a cluster into pions, and then boosts the system back into the lab frame. Figure 47 shows the η and P_T distributions of cluster fragments. The multiplicity of particles in the dissociating system is shown in Figure 48.

The minimum particle pseudorapidity in the dissociating system for all LPAIR events, and the corresponding distribution for events with muon pairs within the acceptance are given in Figure 49. The corresponding plots as a function of muon-pair mass are shown in Figure 50. From the above plots, we count 14.2% events with $\eta_{min} \geq 7.4$. To get the probability of a blind dissociation4, the efficiency of the BSC 3 counters, BSC3 must be taken into account. We have determined the BSC3 efficiency to be 90.10%, we see that in the event that one or both of the beam particles dissociate, 15.8 ± 1.4% of the events will have a blind dissociation, where products fall into $\eta_{min} \geq 7.4$.

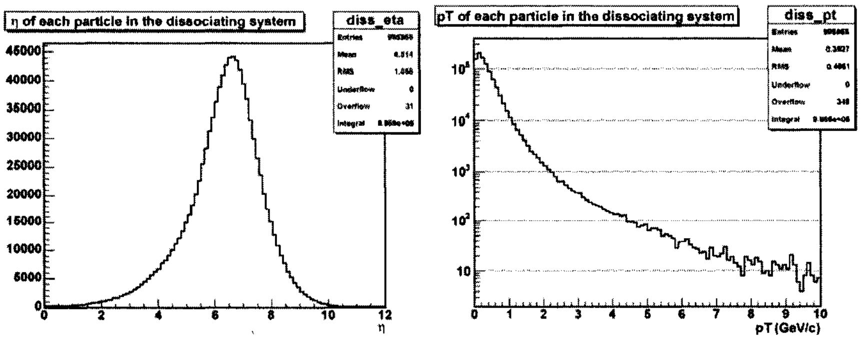

Figure 47: The η and pT distributions of cluster fragments for the simulated events.

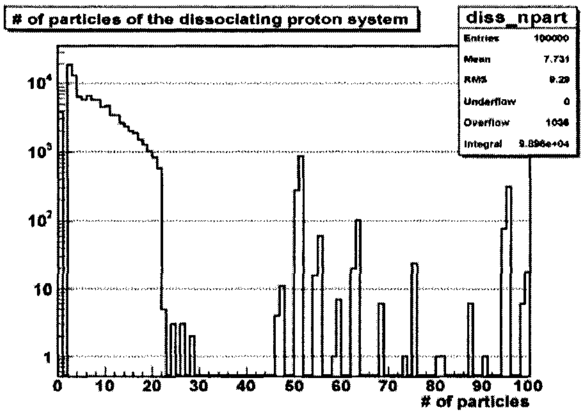

Figure 48: The multiplicity of particles in the dissociated proton/antiproton system.

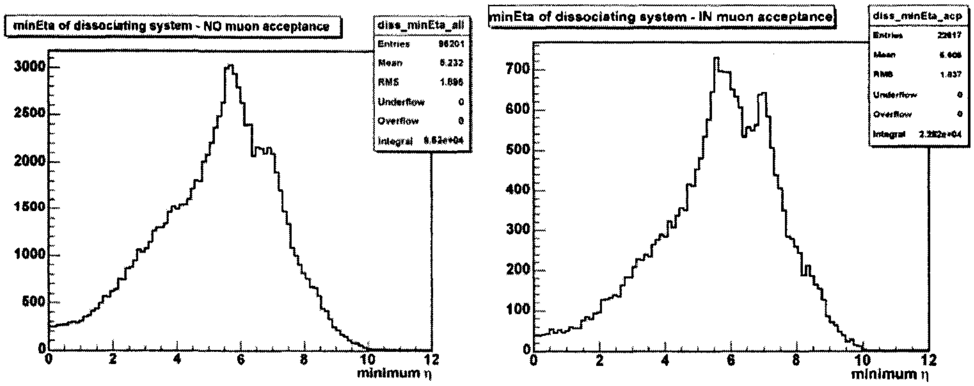

Figure 49. Minimum Eta distribution for with (right) and without (left) muon acceptance cuts.

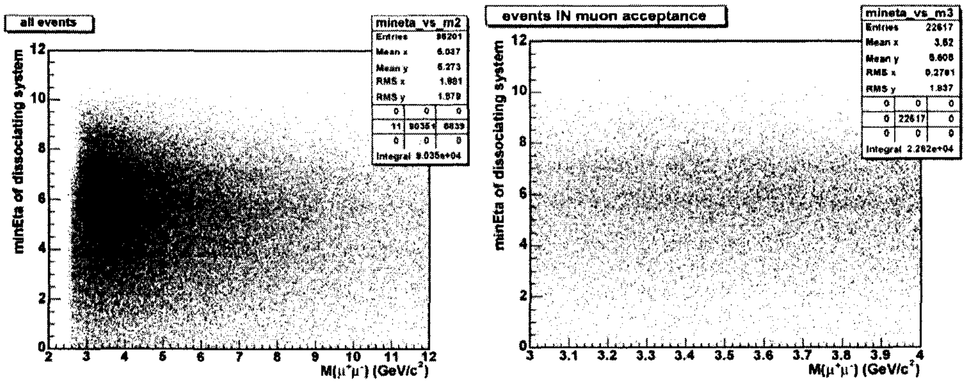

Figure 50. Minimum Eta varying with dimuon mass, for with (right) and without (left) muon acceptance cuts.

	LPAIR cross sections (pb)
σ_{el-el}	**2.19 ± 0.45**
$\sigma_{inel-el}$	**0.74 ± 0.18**
$\sigma_{inel-inel}$	**0.23 ± 0.05**

Table 14. Predicted Cross Sections from LPAIR Mont Carlo

However, proton and/or the antiproton only dissociate in a fraction of the events. One needs to know this fraction in order to estimate the actual dissociation background to our signal. This fraction can be estimated using the inelastic running mode of LPAIR MC using the cross-section shown in Table 14. The total number of QED continuum events that survive the analysis and exclusivity cuts is 77.3 ± 9.6. This number must include the dissociation background. The cross-section for events that blindly dissociate is given by:

$$2 \times p_{minEta\geq7.4} \times \sigma_{inel-el} + (p_{minEta\geq7.4})^2 \times \sigma_{inel-inel} = 0.24\,pb$$

where $p_{minEta\geq7.4} = 15.8\%$. Thus the number of events in the dissociation background is:

$$(77.3 \pm 9.6)\text{events} \times \frac{0.24pb}{\sigma_{el-el} + 0.24pb = 2.43pb} = (7.6 \pm 0.9)\text{ events}$$

4.3.4 Cosmic background

A cosmic ray particle that could potentially mimic the signal will first hit the TOF detector, then travel through the detector near to the interaction point and hit the TOF again on the way out of the detector. The time difference between hits in the TOF will then actually be comparatively long. In practice, the cut ΔTOF $\leq$ 3 ns kills effectively all of the cosmic ray background. The combination of the TOF cuts and the 3D opening angle cuts effectively eliminate all the cosmic background. An inspection of Figure 51 for the candidate dimuon events that survive the analysis cuts and the exclusivity cuts show that there is no excess of events populating the η-sum = 0 regions that would be expected if cosmic ray background remained. Thus, the cosmic ray background is taken to be negligible.

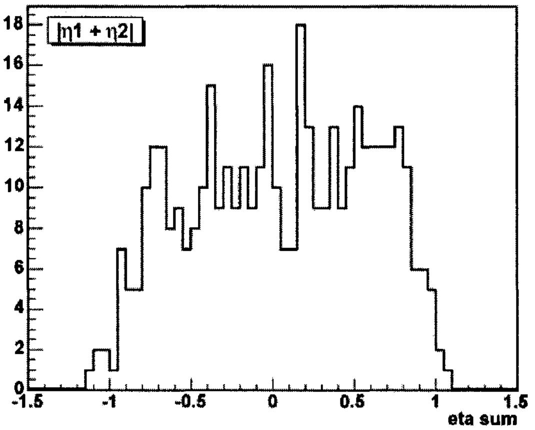

Figure 51. Eta-sum (left) and Charge (right) distribution for the final signal events

Finally Table 15 summarizes all the background processes.

Background	$\gamma\gamma \to \mu^+\mu^-$	$J/\psi \to \mu^+\mu^-$	$\psi' \to \mu^+\mu^-$
χ_c	**N.A.**	**2.8 ± 1.9**	**N.A.**
non-exclusive	**7.0 ± 3.9**	**8.6 ± 8.6**	**8.6 ± 8.6**
cosmic	**0**	**0**	**0**
dissociation	**7.6 ± 0.9**	**28.7 ± 3.4**	**3.9 ± 0.5**
Total	**14.6 ± 4.0**	**15.8 ± 9.4**	**12.5 ± 8.6**

Table 15. Summary of all the backgrounds

4.4 Measured Cross Sections Compared with Monte Carlo Prediction

Based on the observed number of events, efficiencies (Table 10) and backgrounds (Table 15), we calculate the cross sections according to the formula below:

$$Br(\mu\mu) \cdot \sigma_{measured}^{acceptance} = \frac{N_{signal} - N_{bkgd}}{(\varepsilon_{det.rec} \cdot \varepsilon_{L1} \cdot \varepsilon_{Q} \cdot \varepsilon_{cosmic}) \cdot L_{effe}}$$

$$acceptance \to pt \geq 1.4;\ |\eta| \leq 0.6;\ mass \in [3,4]$$

The measured cross sections are list in Table 16. We compared the results with STARLIGHT Monte Carlo predictions which are list in Table 17. Within statistical errors, the cross section for the QED two-photon process agrees with STARLIGHT prediction, and the cross section for the ψ' meson production agree with STARLIGHT prediction too. We note that all our cross sections for QED two-photon process andψ' meson production are about 1σ higher than the predictions. The measured cross section for the J/ψ meson production is larger than the STARLIGHT Monte Carlo prediction.

	$\gamma\gamma \rightarrow \mu\mu$	$J/\Psi \rightarrow \mu\mu$	$\Psi' \rightarrow \mu\mu$
N_{signal}	**77.3 ± 9.6**	**286.5 ± 17.1**	**38.5 ± 6.8**
N_{bkgd}	**14.6 ± 4.0**	**15.8 ± 9.4**	**12.5 ± 8.6**
$N_{signal} - N_{bkgd}$	**62.7 ± 10.4**	**270.7 ± 19.5**	**26.0 ± 11.0**
L_{effe}	$\mathbf{138.6 \pm 8.3\, pb^{-1}}$		
$(\varepsilon_{det.rec} \cdot \varepsilon_{L1} \cdot \varepsilon_{Q} \cdot \varepsilon_{cosmic})$	**17.4 %**	**6.2 %**	**24.0 %**
$Br(\mu\mu) \cdot \sigma_{measured}^{acceptance}$ (pb)	**2.6 ± 0.5**	**31.5 ± 2.9**	**0.78 ± 0.3**
$\sigma_{measured}^{acceptance}$ (pb)	**2.6 ± 0.5**	**531.2 ± 48.9**	**106.8 ± 41.1**

Table 16. Summary of measured cross sections

	$\gamma\gamma \rightarrow \mu\mu$	$J/\Psi \rightarrow \mu\mu$	$\Psi' \rightarrow \mu\mu$
$\sigma_{StarLight}$	$2.4\, nb$	$19.6^{+4.7}_{-1.8}\, nb$	$3.2^{+0.8}_{-0.3}\, nb$
$\frac{d\sigma_{StarLight}}{dy}(y = 0)$		$2.7^{+0.6}_{-0.2}\, nb$	$0.46^{+0.11}_{-0.04}\, nb$
$\sigma_{StarLight}^{acceptance}$	$2.17\, pb$	$329.8^{+79.1}_{-30.3}\, pb$	$119.5^{+29.9}_{-11.2}\, pb$

Table 17. STARLIGHT Monte Carlo predicted cross sections

5. Conclusion

We have observed three different exclusive processes, all for the first time, in hadron hadron collisions: $\gamma\gamma \rightarrow \mu^+\mu^-$; $\gamma\mathbb{P} \rightarrow J/\psi$ or $\psi' \rightarrow \mu^+\mu^-$; $\mathbb{P}\mathbb{P} \rightarrow \chi_c \rightarrow J/\psi + \gamma \rightarrow \mu^+\mu^- + \gamma$. All the measurements are performed within: $pt \geq 1.4\,GeV/c$; $|\eta| \leq 0.6$; $mass \in [3,4]\,GeV/c^2$ at the CDF II detector at Fermilab. The observed cross section for continuum process $\gamma\gamma \rightarrow \mu^+\mu^-$ is consistent with QED expectations. The observation of QED mediated exclusive $\gamma\gamma \rightarrow \mu^+\mu^-$ interaction confirms that it is possible for these interactions to be observed at LHC. This confirmation is a first step toward using QED mediated exclusive $\gamma\gamma \rightarrow \mu^+\mu^-$ interactions for luminosity monitoring and searches for new physics at the LHC. The vector meson production rates are also consistent with QCD expectations and in agreement with HERA measurements [38]. The cross section for $\gamma\mathbb{P} \rightarrow J/\psi \rightarrow \mu^+\mu^-$ does not agree with STARLIGHT MC prediction, this difference is currently being studied, and one possible source might be from the odderon exchange processes.

Bibliography

[1] An Introduction to the Standard Model of Particle Physics,
by Cottingham & Greenwood, Cambridge University Press (1999)
[2] Nucl. Phys. 22, 579 (1961), S. L. Glashow;
Phys. Rev. Lett. 19, 1264, (1967), S. Weinberg,
[3] Phys. Lett. B47, 365 (1973), H. Fritzsch, M. Gell_Mann, H. Leutwyler
Phys. Rev. Lett. 30. 1343 (1973), D. Gross, F. Wilczek
Phys. Rev. Lett. 30, 1346 (1973), H. D. Politzer
[4] Quantum Electrodynamics
by Walter Greiner & Joachim Reinhardt, Springer; 3rd edition (2002)
[5] Phys. Rev. Lett. volume 89, No. 1, 011301 (2002).
Phys. Rev. Lett. volume 92, 181301 (2004).
http://www.sno.phy.queensu.ca/
[6] The Quantum Theory of Fields, by S. Weinberg
Cambridge University Press, Vols. 1-3. , (1995-2000)
[7] hep-ph/9709356 (1999), "A SUSY Primer" by S. P. Martin
[8] Phys. Lett. B 60, 177 (1976) "A Universal gauge theory model based on E_6"
[9] "The Grand Unified Theory" by R. Haynes, Paladin Contemporaries (2001)
[10] "String Theory and M-Theory: A Modern Introduction"
by K. Becker, M. Becker, J. H. Schwarz, Cambridge Press; 1st Edition (2007)
[11] "Introduction to Regge Theory and High Energy Physics".
P.Collins. Cambridge University Press, 1977.
[12] "First Observation of Exclusive Electron Pairs in Hadron-Hadron Collisions" CDF internal note 7930
[13] "Charmonium" M. B. Voloshin, arXiv:0711.4556v1
[14] "Photoproduction of Quarkonium in Proton-Proton and Nucleus-Nucleus Collisions" by S. Klein & J. Nystrand, Phys. Rev. Lett. volume 92, No. 14 (Apr. 2004).
"Photoproduction in Ultra-Peripheral Heavy-Ion Collisions"
by J. Nystrand, arXiv:0710.4027v1 (Oct. 2007)
[15] Nucl. Phys. B229, 347 (1983). J. Vermaseren
Program Library Long Writeup W5013 (1993)
[16] Private communication with J. Stirling
[17] Eur. Phys. Journ. C, 35, Number 2, 211 (2004)
V. Khoze, A. Martin, M Ryskin, W. J. Stirling
[18] "CDF detector simulation framework and performance",
arXiv:physics/0306031v1
[19] http://www-cdf.fnal.gov/cdfsim/cdfsim_main.html

[20] “CERN Program Library Long Writeup W5013”
http://wwwasd.web.cern.ch/wwwasd/geant/
[21] “CDF Run II Handbook”, http://www-bd.fnal.gov/runII/
[22] http://www-bdnew.fnal.gov/operations/lum/lum.html
http://www-cdfonline.fnal.gov/ops/opshelp/stores/
http://www-bd.fnal.gov/pplot/today/DataSummaryTables.html
[23] Phys. Rev. D 51, 4623 (1995), CDF Collaboration;
Physical Review Letters 74: 2422-2426, D0 Collaboration;
Physical Review Letters 74: 2626-2631, CDF Collaboration;
“A Combination of CDF and D0 Results on the Mass of the Top Quark” arXiv:0803.1683;
[24] http://physics.rockefeller.edu/michgall/fd/forward_detectors.html
[25] Patrick T. Lukens. The CDF IIb detector: Technical design report. FERMILABTM-2198.
[26] CDF Internal Note 6362, “The CDF Run I Muon System Upgrade”
[27] CDF Internal Note 5870, “A Guide to Muon Reconstruction and Software for Run II”
[28] “Electron Avalanches and Breakdown in Gases”
Washington Butterworths Advanced Physics Series, 1964
[29] Nucl. Inst. Meth. A 268, 33, 1988
[30] CDF Internal Note 6992, “The COT pattern Recognition Algorithm and Offline Code”
[31] CDF Internal Note 6646, “A Search For Exclusive $J/\psi+\gamma$ Production”
[32] CDF Internal Note 7369, “A Search For Exclusive $J/\psi+\gamma$ Production in data Taken with a diffractive J/ψ trigger”
[33] CDF Internal Note 8307, “Low P_T Muon ID Efficiencies in Data gen6 for Exotics Searches”
[34] CDF Internal Note 7197, “ID efficiency for isolated, intermediate P_T muons”
[35] CDF Internal Note 7314, “Measurement of the Level-1, 2 and 3 Low P_T Dimuon Trigger Efficiencies for the $B_s^0 \to \mu^+\mu^-$ Analysis”
[36] CDF Internal Note 9084, “Measurement of Level-1 CMU Trigger Efficiency for very low-P_T muons”
[37] MBR Monte Carlo, Rockefeller Group, CDF
[38] Vector Meson Cross Sections at HERA, arXiv:0801.1970